SAPIENZA
UNIVERSITÀ DI ROMA

Design and Studying Physical Properties of Cavity Beam Position Monitors for Electron Accelerators

Dr. Daniele Del Re

Dottorato di Ricerca in Fisica – XXXIII Ciclo

Candidate

Shalva Bilanishvili
ID number 1827925

Thesis Advisor

Dr. Massimo Ferrario

Co-Advisor

Dr. Andrea Mostacci

January 2021

Thesis defended on 28 April 2021
in front of a Board of Examiners composed by:

Prof. Pasquale Arpaia (chairman)

Prof. James Rosenzweig

Prof. Giovanni Mettivier

Design and Studying Physical Properties of Cavity Beam Position Monitors for Electron Accelerators

Ph.D. thesis. Sapienza – University of Rome

This thesis has been typeset by LaTeX and the Sapthesis class.

Version: May 5, 2021

Author's email: shalva.bilanishvili@lnf.infn.it

Abstract

The INFN project named EuPRAXIA@SPARC_LAB is a proposal to upgrade the SPARC_LAB test facility (in Frascati, Italy) to a soft X-ray user facility based on plasma acceleration and high-gradient X-band accelerating structures. Furthermore, the European project CompactLight aims to design a compact FEL for users in the hard X-ray range. Its main pillars are a new concept high-brightness photoinjector, high-gradient X-band accelerating sections, and innovative short-period undulators.

The control of the charge and the trajectory at a few pC and few μm is mandatory in this machine, especially in the plasma interaction region.

Great importance has the beam trajectory at the entrance of every RF module, particularly the part of the machine in the X-band and inside the plasma accelerator. Conventional stripline BPM (Beam position monitor), similar to those already in use at SPARC_LAB, can be considered for such a task. They can offer a good signal to noise ratio down to a few pC charge and a resolution in the order of several tens of μm. However, this kind of device can be used only at the beginning of the accelerator, where the beam pipe is 40 mm. However, starting from X band structures, the pipe size decreases. Since one of the most crucial parameters is the device's length, it will be convenient for such a system that length to be as short as possible.

As a possible solution, a cavity beam position monitor (cBPM) is proposed.

A prototype cavity BPM in the C-band frequency range has been designed. This thesis presents the strategy and the process to specify the parameters that are decisive for achieving the required specifications. The simulations were performed to study RF properties and the electromagnetic response of the device. The developed RF design fits the EuPRAXIA project requirements. Other design ideas, such as a single cavity BPM, where both dipole mode and reference signals are received from one cavity, are also discussed. The resonance modes of the cavity are simulated using eigenmode solvers. By the simulations performed in frequency-domain, the coupling and isolation characteristics are obtained. The beam coupling is studied through time-domain simulations. The possible manufacturing errors were studied by simulation reconstruction.

Finally, the performance of the whole system for 5.1 GHz is discussed, and theoretical resolution is approximated.

Contents

Chapter 1

Introduction

1.1 EuPRAXIA @ SPARC_LAB

EuPRAXIA@SPARC_LAB [27], [28] (also named EuSPARC) is the proposal for the upgrade of the SPARC_LAB test facility [29] at INFN-LNF (Frascati, Italy). The ultimate intent is to design and build a new multi-disciplinary user-facility, equipped with a soft X-ray Free Electron Laser (FEL) driven by a $\propto$1 GeV high brightness linac based on plasma accelerator modules. This design research implemented in synergy with the Horizon 2020 Design Study EuPRAXIA (European Plasma Research Accelerator with eXcellence In Applications) [30],[31], and the purpose is to demonstrate exploitation of plasma accelerators for users. The EuPRAXIA@SPARC_LAB project intends to put forward the Laboratori Nazionali di Frascati (LNF) in Italy as a host of the EuPRAXIA European Facility.

In order to achieve aforementioned intent and to meet the EuPRAXIA requirements, some necessary preparatory steps have to be taken at LNF:

To provide LNF with new infrastructure, the size of about 130m$\times$30m, like the one required to host the EuPRAXIA facility, is necessary. To design and build the first-ever 1 GeV X-band RF linac and an upgraded FLAME laser up to the 0.5 PW range with a compact FEL source, equipped with a user beamline $4-2$ nm wavelength, driven by a high gradient plasma accelerator module.

The EuPRAXIA@SPARC_LAB facility by itself will equip LNF with a unique compound of a high brightness GeV-range electron beam generated in a state-of-the-art linac and a 0.5 PW-class laser system. In the case of LNF not being selected and/or of a failure of plasma acceleration technology, the infrastructure will remain top-class quality, user-oriented, and at the vanguard of new acceleration technologies.

The EuPRAXIA@SPARC_LAB project requires constructing a new structure to receive the linac, the FEL, the experimental room, and the support laboratories. The new facility will cover nearly an area of 4000 m^2. The layout of the EuPRAXIA@SPARC_LAB infrastructure is presented schematically in Figure 1.1 From left to right, one can see a 55 m long tunnel hosting a high brightness 150 MeV S-band RF photoinjector, equipped with a hybrid compressor scheme based on both velocity bunching and magnetic chicane. The energy boost from 150 MeV up to a maximum of 1 GeV will be provided by a chain of high gradient X-band rf cavities. A 5 m long plasma accelerator section will be installed at the linac

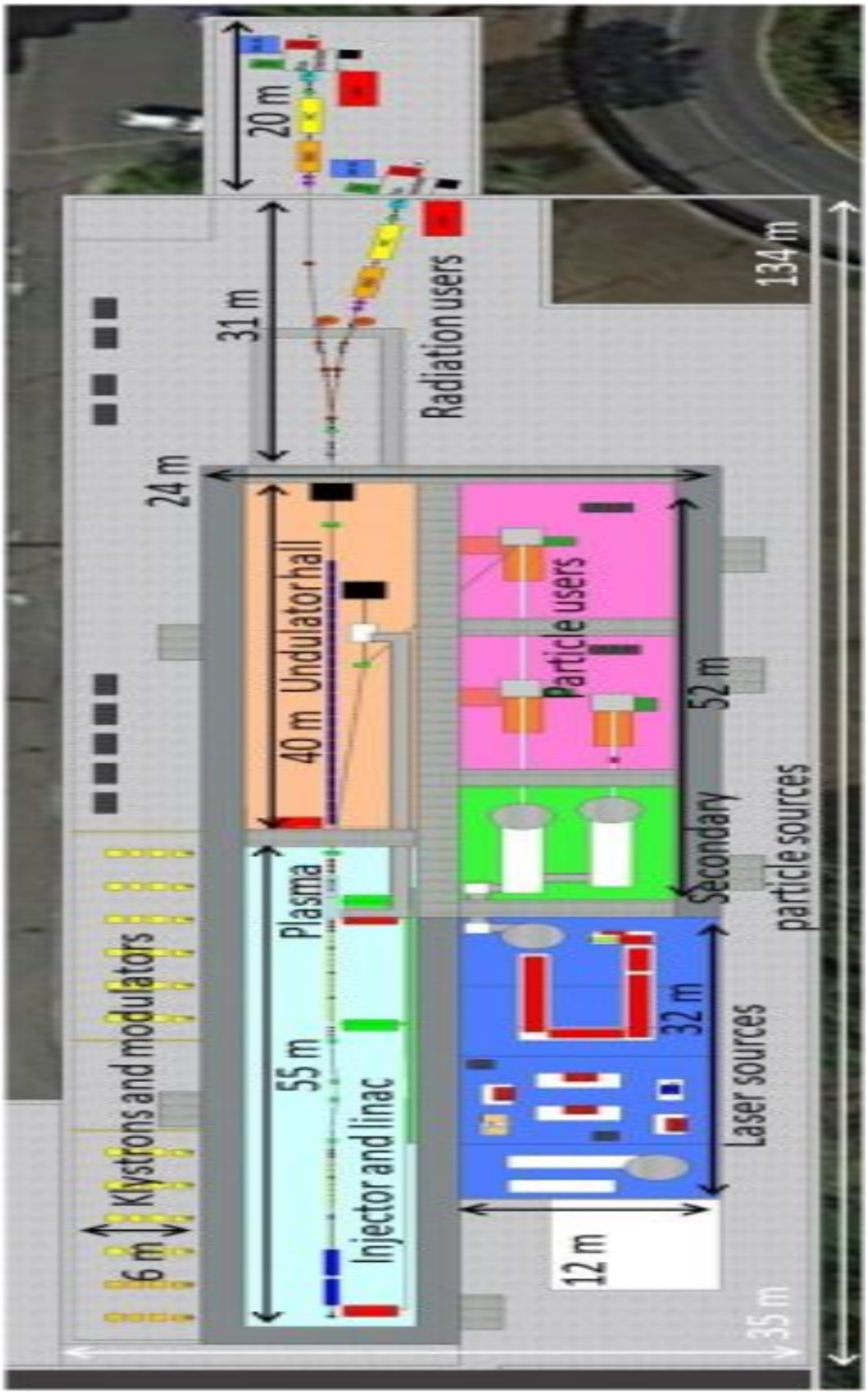

Figure 1.1. EuPRAXIA@SPARC_LAB's infrastructure layout.

Table 1.1. EuPRAXIA@SPARC_LAB's beam parameters for plasma and conventional RF linac driven FEL.

Parameter	Units	Full rf	LWFA	PWFA
Electron energy	GeV	1	1	1
Repetition rate	Hz	10	10	10
RMS Energy Spread	%	0.05	2.3	1.1
Peak Current	kA	1.79	2.26	2.0
Bunch charge	pC	200	30	200(D)-3-(W)
RMS Bunch Length	μ m (fs)	16.7 (55.6)	2.14 (7.1)	3.82 (12.7)
RMS normalized Emittance	mm mrad	0.05	0.47	1.1
Slice Length	μm	1.66	0.5	1.2
Slice Charge	pC	6.67	18.7	8
Slice Energy Spread	%	0.02	0.015	0.034
Slice normalized Emittance (x/y)	mm mrad	0.35/0.24	0.45/0.465	0.57/0.615
Undulator Period	mm	15	15	15
Undulator Strength $K(a_w)$		0.978 (0.7)	1.13(0.8)	1.13(0.8)
Undulator Length	m	30	30	30
ρ (1D/3D)	$\times 10^{-3}$	1.55/1.38	2/1.68	2.5/1.8
Radiation Wavelength	nm (keV)	2.87 (0.43)	2.8 (0.44)	2.98(0.42)
Photon Energy	μJ	177	40	6.5
Photon per pulse	$\times 10^{10}$	255	43	10
Photon Bandwidth	%	0.46	0.4	0.9
Photon RMS Transverse Size	μm	200	145	10
Photon Brilliance per shot	(s mm2 mrad2 bw(0.1%)) $^{-1}$	1.4×10^{27}	1.7×10^{27}	0.8×10^{27}

exit, which combines the plasma module and the required matching and diagnostics sectors. A 40 m long undulator hall is shown in the downstream tunnel, where the undulator chain will be installed. Further downstream, after a 12 m long photon diagnostic section, the user hall is displayed.

Supplementary radiation sources, just like THz and γ-ray Compton sources, are foreseen in the other shown beamlines. The upper room is dedicated to hosting klystrons and modulators. The existing 300 TW FLAME laser, eventually upgraded up to 500 TW, will be installed in the lower light-blue room. The plasma accelerator module can be driven in this layout by an electron bunch driver (PWFA scheme) or by the FLAME laser itself (LWFA scheme). A staged configuration of both PWFA and LWFA schemes will also boost the final beam energy exceeding 5 GeV. Besides, FLAME is assumed to drive plasma targets in the dark-blue room to drive electron, and secondary particle sources available to users in the downstream 30 m extended user area.

The experimental activity's primary focus will be the consummation of plasma in driven short-wavelength FEL with one user beamline, according to the beam parameters reported in Table 1.1. Then EuPRAXIA@SPARC_LAB will provide an FEL radiation spectrum in the so-called "water window", a region where water is transparent to soft X-rays (wavelength of $2.3 - 4.4$ nm). The first anticipated FEL operational mode bases on the Self Amplification of Spontaneous Radiation. (SASE) the principle with tapered undulators. More high-level mechanisms like Seeded and Higher Harmonic Generation compositions will be investigated as well. The user endstation, called EX-TRIM (Eupraxia X-ray Time-Resolved coherent IMaging),

will be designed and built to perform a comprehensive set of experiments. As a specific example of EuPRAXIA@SPARC_LAB applications, it is worth noting that the FEL radiation in the soft X-ray spectrum offers potentialities for novel imaging methodologies and time-resolved researches in medicine, biology, and material science, along with non-linear optics applications.

For example, Coherent Imaging of Biological samples in the water window. Exploiting the FEL beam's coherence and its wavelength falling within the "water window", 2D and 3D images of biological samples in a wet environment can be obtained with high contrast concerning the surrounding medium, meaning that a broad class of biological objects, including protein clusters, viruses, and cells, can be profitably studied.

Laser ablation plasma − Laser ablation/desorption techniques are utilized extensively across diverse disciplines, including the production of new materials and extrinsic and in situ chemical analysis. In the case of ablation, the use of ultra-fast laser pulses provides a powerful means of machining a wide variety of materials, including biological tissue. The absence of thermal relaxation of the energy allows unprecedented precision and practically no associated damage, which has stimulated considerable interest in industrial processes and applications. Electronically induced surface reactions in semiconductors, metal/adsorbate systems, and multiphase composite materials can be investigated.

Condensed Matter − Science Coherent Diffraction Imaging (CDI) experiments tackling many open questions in Condensed Matter Physics. For instance, the quest for smaller and faster magnetic storage units is still a challenge of magnetism. The possibility to study the evolution of magnetic domains with nanometer/femtosecond spatial/temporal resolution will shed light on the elementary magnetization dynamics such as spin-flip processes and their coupling to the electronic system.

Clusters and nanoparticles − particularly great interest, arise in the correlations between the geometric structure and electronic properties of variable size clusters, underlying changes in optical, magnetic, chemical, and thermodynamic properties. In the spectral range from 3 to 5 nm envisaged for the FEL source, physical processes involving core levels are essential.

Pump and probe experiments − For example, resonant experiments with pulses tuned across electronic excitation will open up the way towards stimulated Raman or four-wave mixing spectroscopies.

1.2 Electron beam diagnostics at EuPRAXIA@ SPARC_LAB

The beam diagnostics must be significantly advanced to meet all the diagnostic requirements of the project. The electron beam accelerated by the main linac can be allowed multi-shot measurements, mainly due to the inherent machine stability.

In Table 1.2 are listed the beam transverse and longitudinal parameters for the bunch injected inside the plasma.

At the plasma booster entrance, the beam transverse dimension is about 1 μm rms, and its length is in the order of a few fs. After the plasma acceleration, bunch length and emittance are relatively preserved, but the inherent instability also demands single-shot measurements.

Table 1.2. Beam parameters at plasma entrance.

	Units	@plasma entrance
bunch charge	pC	30
bunch length rms	fs	12
peak current	kA	3
Rep. rate	Hz	10
Rms norm. emittance	μm	0.44
Transverse beam size (rms)	μm	≈ 1

The analysis is divided into three different branches: transverse, longitudinal, charge, and trajectory diagnostics.

1.2.1 Transverse diagnostics

There are two main measurements for transverse diagnostics: emittance and envelope. The envelope is critical to properly match the beam along with the machine, comparing the measured dimensions with the simulated ones. Figure 1.2 shows the horizontal and vertical rms beam sizes.

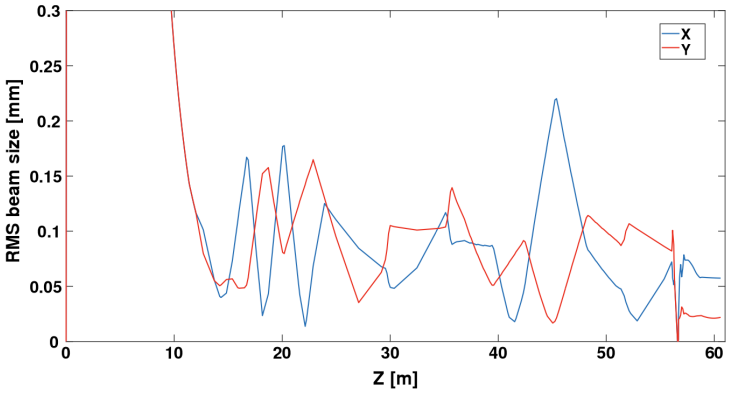

Figure 1.2. Beam envelop evolution along the linac. The transverse dimensions approach μm level at the plasma booster.

Usually, scintillator screens, like YAG:Ce or Optical Transition Radiation (OTR) monitors, are used for such a task. In particular, YAG screens are widely used when the beam charge is below about a few tens of pC, due to their better photon yield. In order to mitigate the problem of the depth of field and the crystal view angle [39], the conventional mounting considers putting the YAG perpendicular to the beamline and a mirror placed at 45° concerning this direction to reflect the radiation at 90° to the beamline. This radiation is then extracted via a vacuum window and imaged on a CCD. Compact design is required in order to preserve the compactness of the whole machine. As an example, in Figure 1.3, a new compact design uses only 40 mm of longitudinal space to host this device.

The emittance measurement can be performed for the main linac with very standard techniques, like quadrupole scan and multiple screens [41]. Though, for

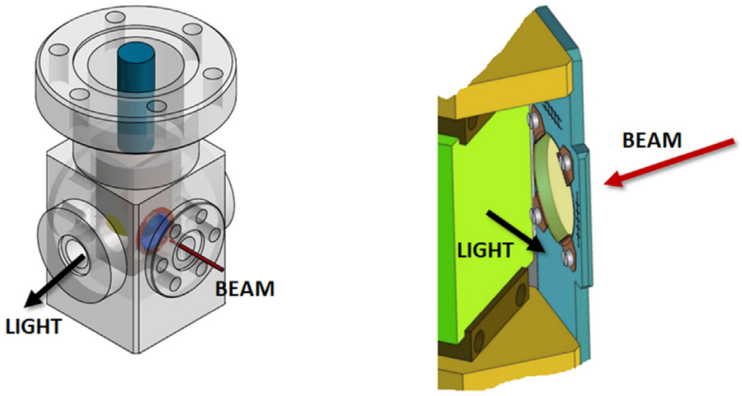

Figure 1.3. Example of a compact design for beam size measurements. The overall length is only 40 mm.

plasma accelerated beams, the inherent shot to shot instabilities, with high beam divergence and the need to separate driver and witness, restrict the use of such a diagnostics just after the plasma channel.

For these reasons, It seems more convenient to use a different approach to measure the beam parameters only inside the plasma channel. No measurements will be performed just after the plasma, leaving space for capture optics. After that, an innovative single-shot measurement must be implemented.

The energy spread must also be kept low as possible because, following [42], even the 6D rms emittance is not preserved in a drift with energy spread, and so the measurement of the emittance is strongly dependent on the measurement position.

The measurement inside the plasma bubble can be performed employing betatron radiation. The diagnostics based on betatron radiation [43] has been developed in recent years in several laboratories, relying on the measurement of the spectrum (for instance, see [44]) or on the diffraction from a knife-edge [45].

However, these systems measured just the beam profile and divergence, neglecting the correlation term. A new algorithm has been developed only recently to retrieve the correlation term [40]. It will deliver a better reconstruction of the phase space, employing the electron and radiation energy spectrum's simultaneous measurement. This method relies on some approximation of the initial phase space of the particle. However, if the beam is injected externally inside the plasma, the initial 6D phase space's knowledge solves this ambiguity.

In Figure 1.4 is reported a reconstructed phase space with this technique. To collect the betatron radiation, we have to separate the radiation from the electron beam with a dipole sooner or later. Unluckily, the beam's trajectory bending produces synchrotron radiation, and its spectrum can overlap with the betatron radiation.

1.2.2 Longitudinal diagnostics

For longitudinal measurements, several possibilities are considered to implement in this project. Longitudinal diagnostics is compulsory to set the exact compression phase in the velocity bunching and recover the induced energy spread correlation.

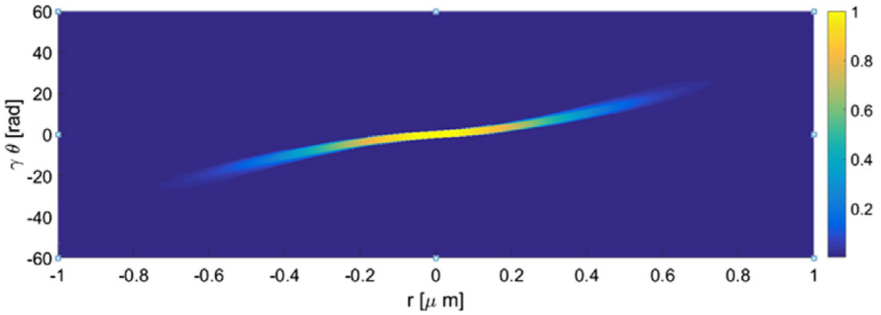

Figure 1.4. Reconstructed phase space with betatron radiation. Parameters are reported in [40]

It is considered okay to use different methods, tailoring the instrumentations to the appropriate machine requirement. The single-shot longitudinal phase space measurement will be performed with an X- band RF deflector (RFD), i.e., an RF cavity with a transverse deflecting mode, combined with a magnetic dipole. The need for an X-band cavity is mainly due to the fs scale resolution attainable in such a way. While this device can reach such a resolution, particular attention is required to its design. The beam can go out of the center inside the device caused by the transverse field. Hence the reduced iris aperture must be considered with beam dynamics simulations. Only one X-band RFD is operating so far at SLAC [46]. It is designed for an energy one order of magnitude greater, so it could be used as a reference, but it must be rescaled, at least in its length.

Nevertheless, for one-shot not intercepting bunch length measurement, useful, for example, when the beam is sent in a plasma module to correlate input and output properties of the bunch, two other systems must be employed. Diffraction radiation emits when a charged particle passes through a hole, with a transverse dimension smaller than the radial extension of the electromagnetic field traveling with the charge. Coherent emission arises when the observed wavelength is longer concerning the bunch length. For our case, where this time length can be in the range between a few ps or few fs, it means to have several detectors, each one sensitive to a range of wavelengths varying from FIR to VIS light. This type of measurement can be employed in multi-shot mode using a Martin Pupplet or Michelson interferometer [47] or a single shot (highly desiderable) dispersing the radiation and collecting it in a linear detector. The complete analysis of the spectrum leads to the reconstruction of the longitudinal bunch shape. There are already several examples of such kind of measurement, using diverse approaches, for example, one based on a single KRS-5 (thallium bromoiodide) prism [48] and another on a series of separate spectrometer working in different wavelength scales [49]. Also, to set the compression phase, sometimes only a relative measurement of the coherent radiation integrated on the detector's whole bandwidth is enough. It is considered to use this compression monitor in almost two positions along with the whole machine. This system can also monitor the phase stability of the section used for compression and eventually stabilize it with feedback.

Another single-shot device based on EOS (Electro-Optical Sampling), described

as the electric field copropagating with the bunch and can rotate a laser impinging polarization on a non-linear crystal GaP or ZnTe. Using a spatial decoding scheme [50], it is possible to retrieve the longitudinal beam profile in one shot. The benefit of such a system regarding coherent radiation is that there is no restoration of the bunch shape starting with frequency analysis, with the problems related to the correct transport and propagation of all the wavelengths in the spectrum. However, the disadvantage is the temporal resolution, limited by the crystal bandwidth or the laser probe's length. Typical values are in the order of 40–50 fs. However, this diagnostics will be essential in our machine because while the X band RFD offers a high resolution for the measurement of very short bunches, i.e., in the fs region, it will not be the best choice for ps bunch length. On the other end, the EOS can easily cover this range of dimensions, not intercepting. Also, it often is used as a bunch of arrival monitors. It is imperative in some plasma acceleration schemes, such as external injection [51].

1.2.3 Charge and trajectory diagnostics

The ability to manipulate the charge and the trajectory at a few pC and a few μm are compulsory in this machine, notably in the plasma interaction region. Bergoz Turbo-ICT (integrated current transformer) can be the best choice for the charge, enabling the measurement of a charge as low as 50 fC.

Concerning the optics, the crucial factor is the beam trajectory at the entrance of every RF module, particularly the part of the machine in the X band and inside the plasma accelerator. Conventional stripline BPM, similar to those already in use at SPARC_LAB, can be considered for such a task. They can offer a sufficient signal to noise ratio down to a few pC charge and a resolution in the order of several tens of μm.

Nevertheless, this kind of device can be used only at the beginning of the accelerator, where the beampipe is 40 mm. However, starting from X band structures, the pipe size reduces. Additionally, one of the most significant parameters is the length of the device. Due to a large number of such a system, its length must be as short as possible. In idea, the longitudinal length of C or X band cavity BPM should not exceed 100 mm, that can be a useful solution for such a task. The possibility to have μm level resolution, even at a deficient charge (few pC), using such short longitudinal space, makes compact cavity BPM very appealing for this project.

1.3 Button beam position monitors

The beam pick-up mainly in use is the so-called button BPM. The pick-up can be thought of as a discontinuity in the vacuum chamber. Typical BPM considers four button-type electrodes mounted on the vacuum. The small button size (typical button diameters 6 - 20 mm) and the short vacuum feedthrough allow for a compact installation at a comparatively low price, thus explaining this pick-up type's proliferation; this is significant given a large amount of BPM locations along with the accelerator. The electrodes' relative gains can be calculated by measuring the electrode signal at several different beam positions. In other words, the device interrupts and diverts into a measuring device a portion of the wall image-charge

induced by the beam. If the beam's trajectory is displaced from the center of the vacuum chamber, the magnetic and electric fields are transformed subsequently, so it gives a possibility to measure the beam position through the relative amplitudes of the induced charge on each button. Such a charge depends on the beam position in a non-linear way, so it is crucial to restoring the beam position accurately to have an effective algorithm to process the obtained data.

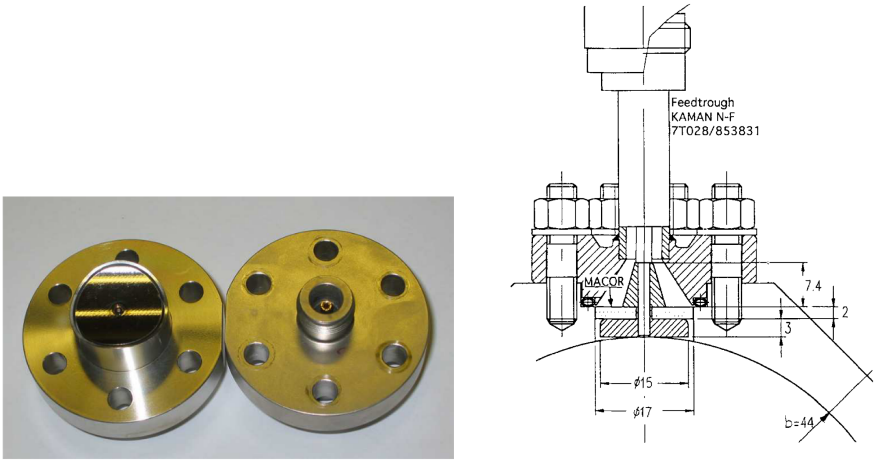

Figure 1.5. Left: photo of a BPM used at the LHC,the air side is equipped witha N-connector[52], Right: BPM button design for the broad-band button electrodes[56]

The button BPM can be considered as a broadband BPM. This type of monitor sensitivity is independent of the frequency. The BPM transfer impedance has typical high–pass characteristics with a cut–off frequency ω_{cut} defined by the pick-up capacity and the matching impedance. For frequencies, $\omega \ll \omega_{cut}$ the voltage drop which is measured across a matched resistor is proportional to the time derivative of the beam current.

1.4 Stripline beam position monitors

One could improve the signal strength even more, for this first logical step would be to increase the device's sensitive area, thus increasing the induced charge. Though, if the bunch length is in the order of the pick-up size, a signal deformation occurs due to the final propagation time. Consequently, the button size should be smaller than the bunch length, which results in insufficient signal strength for short bunches. In this case, stripline BPMs are well suited since the signal propagation is considered in the design, as it is the case for transmission–lines in microwave engineering [59].

Besides, the stripline's azimuthal coverage can be more extensive than that of a button pick-up, thus yielding an increased signal strength. A stripline pick-up consists of an electrode with a length L of several cm, producing a transmission line linking the electrode and the vacuum chamber wall. A signal is induced by the beam at both ends of the line.

The signal depends on the characteristic impedance Z_{strip} of the electrode, which is usually chosen to be 50 Ω. Depending on the downstream port's termination R,

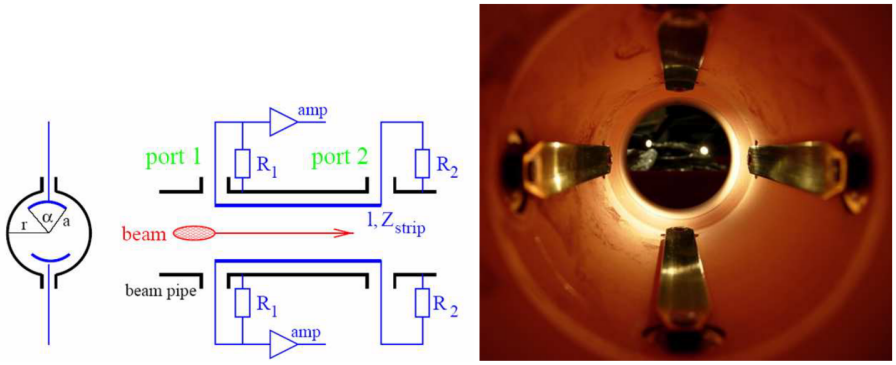

Figure 1.6. Left:Scheme of a stripline pick-up [52]. Right:Photo of the LHC stripline BPM of 12 cm length [52]

the signal there is canceled ($R = Z_{\text{strip}}$) or appears partially ($R \neq Z_{\text{strip}}$). A complete cancellation at the downstream port appears only if the beam's speed is equal to the speed of the signal in the transmission line, which is almost true for $\beta \approx 1$.

It is always possible to extract the induced signal at the upstream port and the reflected inverted one separated in time by $\Delta t = 2L/c$ (for $\beta = 1$). The transfer impedance of a stripline monitor comprises a series of maxima $f_{\text{max}} = c/4L \cdot (2n-1)$ with $n = 1, 2, \cdots$ Therefore, for a given acceleration frequency f_{acc} the length L should be chosen to operate close to such a maximum.

1.5 Specifications and target performance for the cBPM's

The main specifications for the developed cBPM prototype are loaded quality factor Q_L and the working frequency f of the device.

As the indicators for the target performance, one can consider the device's sensitivity and resolution. According to the beam specification of the EuPRAXIA project Table 1.1, the crucial parameters for the prototype, that were provided by the beam instrumentation group, are listed in the Table 1.3

Table 1.3. Specifications for the cBPM.

Parameters	Values
Working frequency range	C band
Loaded quality factor Q_L	≈500
Sensitivity	≈5 V/nC/mm
Required resolution	$< 1\mu$m

Chapter 2

Cavity beam position monitor

The electromagnetic monitor of a beam of charged particles is a conductor system in which a passing beam, giving up part of its energy, excites an electromagnetic field, which is a signal. The field's magnitude and time dependence carry information about the beam intensity and its geometric characteristics, which can be extracted by signal detection. Depending on the structure of the system, the excited field can have the character of a radiation field, standing or traveling waves. The most basic cavity beam position monitor consists of a cavity pick-up, some receiver electronics, and a digital readout. The beam position is determined from the resonant electromagnetic modes. Surface currents necessarily accompany these modes, and so the method of detection is physically no different from the button and stripline BPMs mentioned above. A variety of designs exist for cavity BPMs, but the majority, especially those designed for purposes where a high resolution is needed, include many of the same features. The next two sections give a detailed overview of these features and the underlying physics.

2.1 Calculation of electromagnetic fields induced by a beam

The parameters of the beam of charged particles can be determined by measuring the force with which the electromagnetic field induced by the moving particles of the beam acts on a test charge. The conduction electrons of the substance - conductor are used as test charges. The interaction of a charged particle and a conductor is based on the phenomena of electrostatic and electromagnetic induction, which are manifested in the separation of positive and negative charges present in the conductor in equal amounts. The separation occurs under the influence of the potential electric field of the particle and the vortex electric field arising from the change in time of the magnetic field due to its motion. The distribution of the induced charges and currents is set so that the resulting electromagnetic field inside the conductor is zero. This distribution depends on the shape and location of the conductors, as well as on the magnitude and direction of the particle velocity. In the case of a collection of particles, the electromagnetic field is determined by the superposition of fields from each particle, the distribution of induced charges and currents depends on the number of particles and their position in space.

For the calculations for electromagnetic monitors, the model of an infinitely thin beam is often used:

$$\vec{j}(x,y,z,t) = \vec{v}\rho_z(z+vt)\delta(x-x_0)\delta(y-y_0) \tag{2.1}$$

where δ is the Dirac delta function. Such a beam is characterized by transverse coordinates x_0, y_0 and a linear charge density $\rho_z(z)$ with a characteristic longitudinal size σ_z. In the process of calculating the monitor signals, a beam with an arbitrary transverse particle distribution can be represented as a set of infinitely thin beams. The processes of electrostatic and electromagnetic induction in vacuum are described by Maxwell's equations:

$$\begin{aligned} \vec{\nabla}\cdot\vec{E} &= \frac{\rho}{\epsilon_0}, \qquad & \vec{\nabla}\times\vec{E} &= -\mu_0\frac{\partial\vec{H}}{\partial t}, \\ \vec{\nabla}\cdot\vec{H} &= 0, \qquad & \vec{\nabla}\times\vec{H} &= \vec{J}+\epsilon_0\frac{\partial\vec{E}}{\partial t}. \end{aligned} \tag{2.2}$$

which relate the electric $\vec{E}$ and magnetic $\vec{H}$ fields with the charge density ρ and the current density j of the beam. In the SI system ϵ_0 and μ_0, respectively, the dielectric and magnetic permeability of vacuum, related by the relation $\sqrt{\epsilon_0\mu_0} = 1/c$, where c is the speed of light in vacuum. These equations are supplemented by the boundary conditions relating charges, currents and fields on the surface of the conductors, as well as by the initial conditions.

Calculation of an electromagnetic beam monitor consists in calculating the dependence of the monitor output signals, such as voltages, currents, charges, on the beam parameters. In the calculations of electromagnetic fields induced by a moving beam, an essential role is played by the surrounding structure, which determines the boundary conditions. In addition, the region of interaction of the beam with the electromagnetic monitor is a relatively small area of the equilibrium orbit. Therefore, in this case, the mathematical method of the Green's functions is convenient for calculating the fields induced by the beam [5].

In mathematics, the Green's function is used to solve inhomogeneous differential equations. In signal theory, for the analysis of dynamic systems, an analog of the Green's function; the impulse transient function is widely used , which is the response (output signal) of the system to the input signal in the form of the Dirac delta function.

To calculate the electromagnetic field induced by a singly passing beam, we subject Maxwell's equations Equation 2.2 to the Laplace transform.

$$F(t) = \int_0^\infty f(t)e^{-pt}\mathrm{d}t \tag{2.3}$$

assuming that the fields are equal to zero by the arrival of the bunch:

$$\begin{aligned} \vec{\nabla}\cdot\vec{E} &= \frac{\rho}{\epsilon_0}, \qquad & \vec{\nabla}\times\vec{E} &= -\mu_0 p\frac{\partial\vec{H}}{\partial t}, \\ \vec{\nabla}\cdot\vec{H} &= 0, \qquad & \vec{\nabla}\times\vec{H} &= \vec{J}+\epsilon_0 p\frac{\partial\vec{E}}{\partial t}. \end{aligned} \tag{2.4}$$

where $p = \sigma + i\omega$ is the complex frequency, and ρ and j are determined by the beam. From Maxwell's equations, taking into account the boundary conditions, one can obtain expressions for the electric and magnetic fields in terms of Green's functions. Calculating $\vec{E}$ from the second equation of system Equation 2.4 and substituting it into the first equation, we obtain the equation for the magnetic field $\vec{H}$ (the inhomogeneous Helmholtz equation):

$$\nabla^2 \vec{H} - p^2 \mu_0 \epsilon_0 \vec{H} = -\nabla \times \vec{j} \tag{2.5}$$

Together with the condition $\vec{H} = 0$ and the specified boundary conditions, this equation determines the magnetic field:

$$\vec{H}(\vec{r}, p) = -\iiint_V G_h(\vec{r}, \vec{r}', p) \nabla \times \vec{j}(\vec{r}', p) \mathrm{d}x' \mathrm{d}y' \mathrm{d}z' \tag{2.6}$$

The integral is taken over the entire area, where $\vec{j} = 0$, $G_h(\vec{r}, \vec{r}', p)$ is the Green's tensor function of the observation point $\vec{r} = (x, y, z)$ and the source point $\vec{r}' = (x', y', z')$ defined by the equation:

$$\nabla_r^2 G_h - p^2 \mu_0 \epsilon_0 G_h = \mathrm{I}\delta(\vec{r} - \vec{r}'), \tag{2.7}$$

where I is the unit tensor. The Green's function $G_h(\vec{r}, \vec{r}', p)$ must satisfy the equation $\nabla G_h = 0$ and the given boundary conditions.

Substituting $\vec{H}$ in Equation 2.6 into the Laplace-transformed Maxwell equations Equation 2.4 and introducing the electric vortex Green's function:

$$G_e(\vec{r}, \vec{r}', p) = -\frac{1}{p\epsilon_0} \nabla_r \times \nabla_{r'} \times G_h(\vec{r}, \vec{r}', p) \tag{2.8}$$

we get an expression for the electric field:

$$\vec{E}(\vec{r}, p) = -\iiint_V G_e(\vec{r}, \vec{r}', p) \nabla \times \vec{j}(\vec{r}', p) \mathrm{d}x' \mathrm{d}y' \mathrm{d}z' - \frac{1}{p\epsilon_0} \vec{j}(\vec{r}', p). \tag{2.9}$$

The last term in Equation 2.9 is due to the space charge of the beam and does not depend on the boundary conditions, therefore, when studying the coherent interaction of the beam with the surrounding structure, it can be omitted.

Equations Equation 2.6 and Equation 2.9 represent the solution of the direct diagnostic problem, i.e., the determination of electromagnetic fields in a monitor of a given configuration, induced by a beam with known parameters. In a number of the simplest cases, these equations can be solved analytically, but for real beam monitors, which are devices of a rather complex configuration, only a numerical solution is possible. In calculating the fields excited by a beam, the Green's function, taking into account the boundary conditions, can be expanded in a series in small deviations in the vicinity of the equilibrium orbit and expressed in terms of the system impedances reduced to the interaction region. It is also believed that charges, currents and fields in the conductor system do not affect the beam. For relativistic beams, this condition is a natural consequence of the causality principle.

An electromagnetic beam monitor is usually an electrodynamic system of one of the following basic types:

Resonators are systems in which the dissipation of electromagnetic energy for one period of oscillation is small compared to the energy stored in them. Standing waves can be excited by the beam in such sensors.

Waveguides are systems in which traveling waves can exist. If the sensor is a two or multiply connected waveguide and its transverse dimensions are small compared to the bunch length, then the beam can excite propagating waves of the transverse (TEM) type only.

Quasistatic systems in which the fields are close to static. Such systems include all kinds of electrode devices, the dimensions of which are small compared to the wavelength excited by the beam, as well as waveguides at a frequency below the critical one.

The listed systems do not exhaust all possible types, but are the most common.

2.1.1 Cavity monitor properties

An electromagnetic resonator is a closed volume with conducting walls, inside which standing waves, excited by a passing beam, can exist. The lossless resonator has a system of eigenvector orthogonal functions $\vec{E}_k(\vec{r}), \vec{H}_k(\vec{r})$ describing vibration modes (standing waves) and connected by a pair of Maxwell equations:

$$\nabla \times \vec{E}_k = -\mu_0 p_k \vec{H}_k \qquad \nabla \times \vec{H}_k = \epsilon_0 p_k \vec{E}_k \tag{2.10}$$

where p_k are the eigenvalues of the wave equation

$$\nabla^2 \vec{H} - p^2 \mu_0 \epsilon_0 \vec{H} = 0 \tag{2.11}$$

Green's function $G_h(\vec{r}, \vec{r}', p)$ is expressed in terms of these eigenfunctions, and the electric field (Laplace image) has the form:

$$\begin{aligned}\vec{E}(\vec{r}, p) = &\sum_k \frac{p}{p_k^2 - p^2} \frac{\vec{E}_k(\vec{r})}{\epsilon_0 \iiint\limits_V \vec{E}_k^2 \mathrm{d}x'\mathrm{d}y'\mathrm{d}z'} \iiint\limits_V \vec{E}_k(\vec{r}')\vec{j}(\vec{r}', p)\mathrm{d}x'\mathrm{d}y'\mathrm{d}z' + \\ &+ \frac{1}{p}\sum_k \frac{\vec{E}_k(\vec{r})}{\epsilon_0 \iiint\limits_V E_k^2 \mathrm{d}x\mathrm{d}y\mathrm{d}z} \iiint\limits_V \vec{E}_k(\vec{r}')\vec{j}(\vec{r}', p)\mathrm{d}x'\mathrm{d}y'\mathrm{d}z' - \\ &- \frac{1}{p\epsilon_0}\vec{j}(\vec{r}, p)\end{aligned} \tag{2.12}$$

In this expression, the first term is the sum of resonant modes, the rest are quasistatic nonresonant fields. The second term describes the expansion of the quasistatic field in resonant vibration modes.

2.2 Beam position monitor

The simplest resonator beam position monitor is a cylindrical resonator, schematically shown in Figure 2.1. A beam flying along the axis of the resonator with a transverse displacement excites the TM110 dipole vibration mode. The amplitude of this mode is proportional to the intensity of the beam and its transverse displacement from the axis [1]. The signal of such a sensor has good linearity, and its amplitude is much higher than that of other electromagnetic sensors, which makes it possible to measure the position of the beam with a submicron accuracy [2],[3].

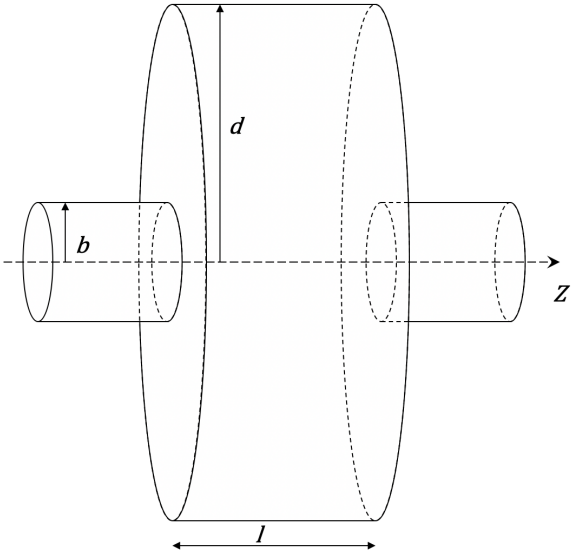

Figure 2.1. A cylindrical cavity sketch.

2.2.1 Signal calculation

Following [1], we consider the excitation of a cylindrical resonator by a beam, assuming that the perturbation of the field configuration by the beam and signal output devices is negligible. If the beam moves along the axis of the resonator, then only TM oscillation modes are excited in the resonator with a nonzero longitudinal component of the electric field $E_z \neq 0$. The electric E and magnetic H fields of the TM_{mnj} mode are described by the following expressions in the cylindrical coordinate system (r, θ, z):

$$\begin{aligned}
E_r &= -C_{mnj}\frac{k_z}{k_r}J_{\prime}^{m}(k_r r)\cos(m\theta)\sin(k_z z)e^{i\omega t},\\
E_\theta &= C_{mnj}\frac{k_z m}{k_r^2}\frac{J_m(k_r r)}{r}\sin(m\theta)\sin(k_z z)e^{i\omega t},\\
E_z &= C_{mnj}J_m(k_r r)\cos(m\theta)\cos(k_z z)e^{i\omega t},\\
H_r &= -iC_{mnj}\frac{\omega\epsilon_0 m}{k_c^2}\frac{J_m(k_c r)}{r}\sin(m\theta)\cos(k_z z)e^{i\omega t},\\
H_\theta &= -iC_{mnj}\frac{\omega\epsilon_0}{k_c}J_m^{'}(k_c r)\cos(m\theta)\cos(k_z z)e^{i\omega t},\\
H_z &= 0.
\end{aligned} \tag{2.13}$$

Where C_{mnj} is the mode amplitude; $k_c = \alpha_{mn}/d$ is the critical wave number; $k_z = j\pi/l$; α_{mn} is the n-th root of the Bessel function of the first kind J_m; d is the resonator radius; l - length; m, n, j is the number of variations in angular θ, radial r and longitudinal z coordinates, respectively; ω is the natural frequency of the TM_{mnj} mode, equal to

$$\omega_{mnp} = c\sqrt{\left(\frac{\alpha_{mn}}{d}\right)^2 + \left(\frac{\pi j}{l}\right)^2}. \tag{2.14}$$

The electromagnetic energy in the resonator passes from the electric field to the magnetic field and vice versa, the total energy accumulated in the resonator is equal to:

$$W = \langle W_E \rangle + \langle W_H \rangle = 2 \langle W_E \rangle \tag{2.15}$$

For each oscillation mode, the resonator can be represented in the form of an equivalent oscillatory circuit, which includes capacitance and inductance, and in a resonator with losses, there is also an active resistance. Equivalent electric circuit of the resonator is a parallel connection of equivalent oscillatory circuits for all modes. The equivalent parameters of the n-th mode R_n, L_n, and C_n are related to the resonator parameters that do not depend on the intensity of the electromagnetic field, such as the resonant frequency of this mode

$$\omega_n = \frac{1}{\sqrt{L_n C_n}} \tag{2.16}$$

shunt impedance

$$R_n = \frac{\left| \int_0^l E_z e^{i\omega_n t} \mathrm{d}z \right|^2}{2P_n} = \frac{V_n^2}{2P_n} \tag{2.17}$$

and quality factor

$$Q_n = \frac{\omega_n W_n}{P_n} \tag{2.18}$$

where W_n is the total accumulated energy of this mode; P_n is the power dissipated by the wall resistance. In a lossy resonator, the accumulated energy decreases exponentially with time:

$$W_n = W_{n0} exp\left(-\frac{\omega_n}{Q_n} t\right). \tag{2.19}$$

The resonant frequency and Q factor determine the decay time of the amplitude of free oscillations in the resonator.

$$\tau_n = \frac{2Q_n}{\omega_n}. \tag{2.20}$$

To output signals from the resonator, communication devices are used, such as a loop interacting with a magnetic field, a whip antenna interacting with an electric field, or a hole in the wall through which an electromagnetic wave enters the output waveguide. The geometric dimensions and position in the resonator of communication devices determine the value of the coupling coefficient, which is equal to the ratio of the output power to the power loss:

$$\beta = \frac{P_{out}}{P_n} = \frac{Q_n}{Q_{load}} - 1, \tag{2.21}$$

where Q_{load} is the loaded quality factor equal to

$$Q_{load} = \frac{Q_n Q_{ext}}{Q_n + Q_{ext}} = \frac{Q_n}{1+\beta}, \tag{2.22}$$

and Q_{ext} is the external figure of merit, defined as the ratio of the stored energy to the energy consumed by the external load [8].

In accelerator technology, resonators are widely used as energy sources for accelerating particles. The integral of the electric field in the cavity, taken along the beam trajectory, gives an accelerating voltage acting on the beam:

$$V_a = \int \vec{E} \cdot \vec{v_b} \mathrm{d}t, \tag{2.23}$$

where v_b is the beam velocity. If the electric field is parallel to the beam velocity, then the accelerating voltage can be written as

$$V_a = \int\limits_{-\infty}^{\infty} E_z e^{i\omega t} v_b \mathrm{d}t = \int\limits_{-\infty}^{\infty} E_z e^{ikz} \mathrm{d}z \tag{2.24}$$

This voltage depends on the field intensity and the effective length of the resonator, which is the product of the geometric length and the transit time factor T_{tr}, taking into account the field change over time of passing beam. For a relativistic beam ($v_b = c$) the transit factor is

$$T_{tr} = \frac{\int\limits_0^l E_z e^{ikz} \mathrm{d}z}{\int\limits_0^l E_z \mathrm{d}z} = \frac{\sin\eta}{\eta}, \quad \text{where} \quad \eta = \frac{\pi l}{\lambda_{mn0}} \tag{2.25}$$

λ_{mn0} is the wavelength of the TM_{mn0} mode. Assuming the field constant along the z axis, we obtain $V_a = E_z T_{tr} l$.

The energy lost by the beam to excite the $n-th$ mode of the resonator can be expressed in terms of the equivalent retarding potential proportional to the voltage of the excited mode. According to the main theorem on the beam loading, the total mode voltage V_n induced by the beam in the resonator is equal to twice the voltage V_a acting on the beam (for the proof of the theorem, see, for example, [4]). Using the definitions of the shunt impedance R_n Equation 2.17 and the quality factor Q_n Equation 2.18 of the $n-th$ mode, the voltage induced by the beam in the resonator can be expressed in terms of the parameters of the equivalent oscillatory circuit

$$V_n = q_b \frac{\omega_n}{2} \left(\frac{R}{Q}\right)_n, \tag{2.26}$$

where q_b is the beam charge; ω_n is the natural frequency, and $(R/Q)_n$ is the normalized shunt impedance of the mode [25].

A beam moving along the resonator axis (r = 0) excites the TM_{010} mode with the largest critical wavelength, m = 0 means that the electric field does not depend on the angle θ. When the beam is displaced along r, the excitation of this mode is weaker, but the next in frequency mode TM_{110} begins to be excited, in which the longitudinal electric field on the resonator axis is zero.

The TM_{110} dipole mode has the maximum amplitude among all beam position-dependent modes (dipole, quadrupole, etc.). The longitudinal electric field of the TM_{110} mode, excited by a beam with coordinates $r = x_0, \theta = 0$, is described by the expression:

$$E_z = C_{110} J_1 \left(\alpha_{11} \frac{x_0}{d}\right) \cos(\theta) e^{i\omega_{110} t}, \qquad \omega_{110} = c\frac{\alpha_{11}}{d} \tag{2.27}$$

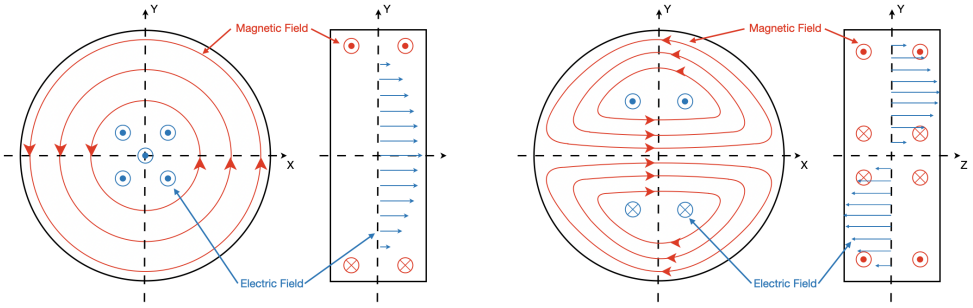

Figure 2.2. The electromagnetic fields of the first monopole (left) and dipole (right) modes in a pillbox cavity

where $\alpha_{11} = 3.832$ is the first root of the Bessel function J_1. As seen from Equation 2.27, the longitudinal electric field of the TM_{110} mode is proportional to the Bessel function J_1 on the radial displacement of the beam, normalized to the cavity radius. The graphs of the Bessel functions J_0 and J_1 are shown in Figure 2.3

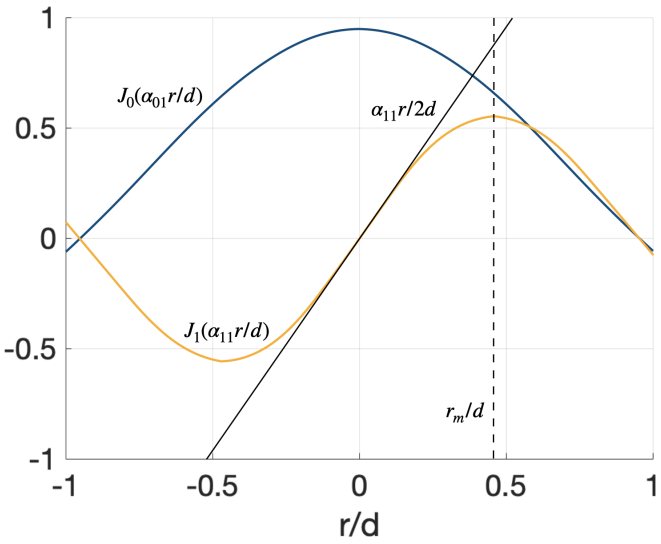

Figure 2.3. Bessel functions J_0 and J_1

The quality factor of the TM_{110} mode can be expressed as

$$Q_{110} = \frac{\lambda_{110}}{2\pi\delta_s}\frac{\alpha_{11}}{1 + d/l}, \tag{2.28}$$

where $\lambda_{110} = 2\pi c/\omega_{110}$ is the wavelength; δ_s is the thickness of the skin layer of the material of the resonator walls with resistivity ρ and magnetic permeability μ:

$$\delta_s = \sqrt{\frac{2\rho}{\mu\omega}}. \tag{2.29}$$

Since the normalized shunt resistance $(R/Q)_n$ is proportional to the square of the radial coordinate, calculations typically use the value $(R/Q)_n$ for a specific offset,

which can be scaled accordingly. The value $(R/Q)_n$ at the radius $r_m \simeq 0.481d$, corresponding to the maximum value of the longitudinal electric field of the mode Figure 2.3, is calculated as

$$\frac{R}{Q}_{110} = \frac{V_{110}^2(r_m)}{2\omega_{110}W_{110}} = \frac{2Z_0 l J_{1max}^2 T_{tr}^2}{\pi\alpha_{11} d J_0^2(\alpha_{11})} \tag{2.30}$$

where $Z_0 \simeq 377\Omega$ - free space impedance; $J_{1max} \simeq 0.582$ - value of the Bessel function at maximum.

The voltage of the TM_{110} mode, excited by a beam flying along the cavity axis with a transverse displacement along the x axis ($\theta = 0$) equal to x_0, can be expressed in terms of the beam charge q_b and the normalized shunt resistance $(R/Q)_{110}$ [19]. As follows from Equation 2.26,

$$\frac{V_{110}(x_0)}{V_{110}(r_m)} = \frac{J_1\left(\alpha_{11}\frac{x_0}{d}\right)}{J_{1max}} \tag{2.31}$$

and, using Equation 2.26, we obtain:

$$V_{110}(x_0) = \frac{q_b\omega_{110}}{2}\frac{J_1\left(\alpha_{11}\frac{x_0}{d}\right)}{J_{1max}}\left(\frac{R}{Q}\right)_{110}. \tag{2.32}$$

For small arguments, the Bessel function $J_1(x)$ can be replaced by $x/2$, thus, the dependence of the voltage V_{110} on the transverse displacement of the beam x_0 is linear in the region bounded by the radius $b \ll d$ of the input and output holes:

$$V_{110}(x_0) = \frac{q_b\omega_{110}}{4}\frac{\alpha_{11}}{J_{1max}}\frac{x_0}{d}\left(\frac{R}{Q}\right)_{110} = q_b x_0 \frac{l T_{tr}^2}{d^3}\frac{Z_0 c \alpha_{11} J_{1max}}{2\pi J_0^2(\alpha_{11})}. \tag{2.33}$$

Expression

$$M_b = \frac{\alpha_{11}}{2J_{1max}}\frac{x_0}{d} \tag{2.34}$$

called the coupling coefficient of the resonator with the beam. Comparing the

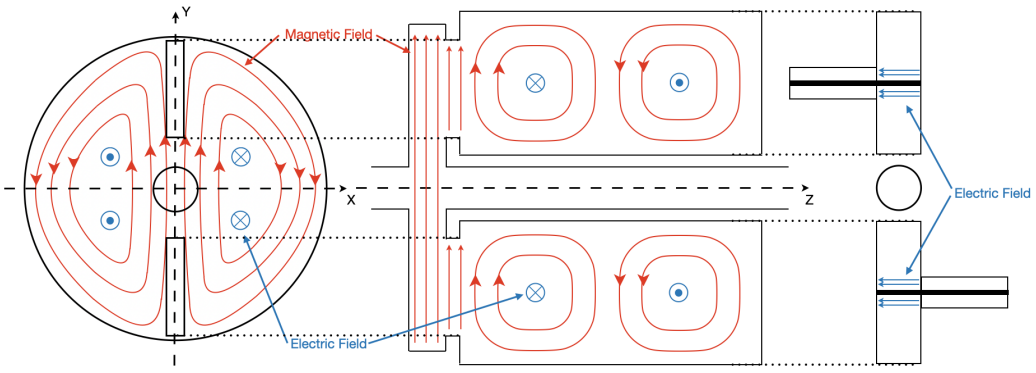

Figure 2.4. Coupling mechanism of the position cavity, waveguide and antenna

magnitude of the signal Equation 2.33 with the rms amplitude of the thermal noise $V_{noise} = \sqrt{4kR\Delta fT}$ (k is the Boltzmann constant, T is the absolute temperature)

in the signal bandwidth Δf, one can estimate the limiting noise resolution of the sensor.

Using two identical communication devices for signal output (loop or pin) located on the $x-$axis ($\theta = 0, \pi$) or y ($\theta = \pm\pi/2$), it is possible to register two independent oscillations of the same mode, excited by a beam displaced from the resonator axis by $r_0 = x_0 + y_0$.

If the resonator is excited by a periodic pulsed beam (cyclic accelerator or multi-bunch mode in a linear accelerator), then a stationary oscillation mode is established in the resonator. In this case, the power output through a coupling device with an external quality factor Q_{ext} can be expressed in terms of the average beam current I_b:

$$P_{out} = I_b^2 M_b^2 \frac{Q_{load}\beta}{1+\beta} \left(\frac{R}{Q}\right)_{110}, \tag{2.35}$$

where Q_{load} is the loaded quality factor Equation 2.22. The signal voltage across the load with resistance R_{load} is $V_{out} = \sqrt{P_{out} R_{load}}$. Upon excitation by a single-incident beam, free oscillations arise in the cavity, which decay with a characteristic time τ_{110} Equation 2.20.[10] The corresponding loaded quality factor Q_{load} is determined from the condition of complete damping of oscillations by the time of arrival of the next beam.

2.2.2 Spatial resolution

Since the maximum of the longitudinal electric field of the in-phase mode TM_{010} is located on the axis of the cavity, this mode is excited much more strongly at small transverse displacements of the beam than the useful mode TM_{110}. Excitation of the TM_{010} mode at its natural frequency ω_{010} can be calculated from Equation 2.13 similarly to the calculation performed for the TM_{110} mode. The ratio of the amplitudes of the modes TM_{110} and TM_{010} is estimated using the expression:

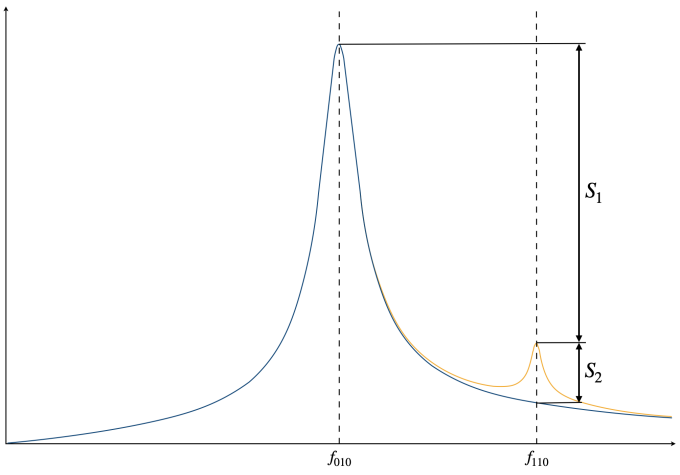

Figure 2.5. Signal spectrum of the cavity

$$S_1 = \frac{V_{110}(\omega_{110})}{V_{010}(\omega_{010})} = \frac{\alpha_{11}}{2J_{1max}} \frac{x_0}{d} \frac{\omega_{110}\left(\frac{R}{Q}\right)_{110}}{\omega_{010}\left(\frac{R}{Q}\right)_{010}} = \frac{\alpha_{11}^2}{2\alpha_{01}J_{1max}} \frac{x_0}{d} \frac{\left(\frac{R}{Q}\right)_{110}}{\left(\frac{R}{Q}\right)_{010}} \tag{2.36}$$

Due to the different natural frequencies of the modes, the main method of suppressing the common mode of the TM_{010} is band-pass filtering of the signal. However, due to the finite Q factor, the TM_{010} mode has a nonzero amplitude at the natural frequency of the TM_{110} mode, as shown in Figure 2.5.

The voltage ratio of the TM_{110} and TM_{010} modes at the frequency ω_{110} can be estimated by the formula:

$$S_2 \simeq S_1 Q_{load} \left(1 - \frac{\omega_{010}}{\omega_{110}}\right). \tag{2.37}$$

The signals of the TM_{110} and TM_{010} modes are compared at a certain distance δx_{min} from the center, which determines the spatial resolution of the resonator sensor:

$$\delta x_{min} \simeq \frac{d}{2Q_{load}} \frac{\omega_{010}\left(\frac{R}{Q}\right)_{010}}{\omega_{110}\left(\frac{R}{Q}\right)_{110}} \tag{2.38}$$

An additional error in the measured coordinate arises if the beam flies through the resonator at an angle x'. In this case, the additional coupling coefficient of the resonator with the beam, due to the nonparallelism of the beam trajectory and the resonator axis, looks like:

$$M_b' = \frac{\alpha_{11}^2 l^2 x'}{12 J_1(\alpha_{01}) d^2} \tag{2.39}$$

and leads to an error in the coordinate equal to [1]

$$\frac{\delta x}{x'} = \frac{\alpha_{11}^2}{12 J_1(\alpha_{01}) \sin\left(\pi \frac{l}{\lambda_{110}}\right)} \frac{l^3}{d^2 \lambda_{110}} \frac{mm}{mrad} \tag{2.40}$$

Thus, the output signal of the resonator at the frequency ω_{110}, in addition to the

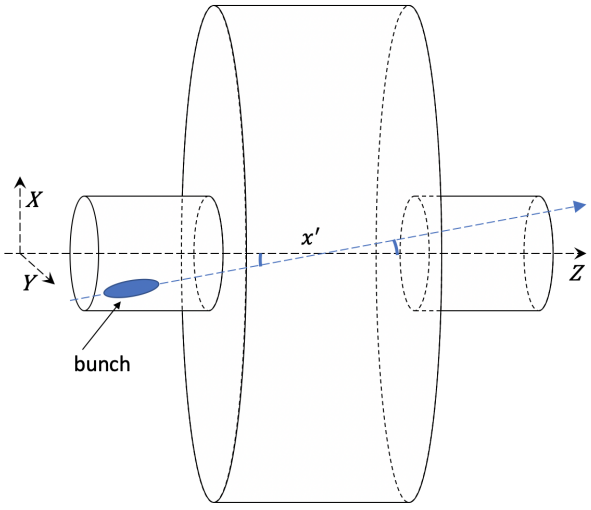

Figure 2.6. Charged particles single bunch crossing cavity with a trajectory angle $x^{'}$.

useful signal of the TM_{110} mode, contains: parasitic signals of the in-phase modes;

signal due to the flight angle x' [3]; as well as electronics noise. When diametrically opposite communication devices are used, the TM_{010} and TM_{110} signals are 180° out of phase relative to each other; in this case, the in-phase modes can be suppressed using sum-difference circuits. The spurious signal from a nonzero flight angle has a phase shift of 90° and can be filtered using synchronous detection. If the residual phase error of the system is small, then the resolution is mainly determined by the thermal noise of the electronics.

2.2.3 Signal processing

In most cases, the resonant frequency of the monitor is on the order of a few GHz, so the signal is processed by high-frequency electronics. The signal output from the resonator by means of coupling devices is a sinusoid with the frequency of the TM_{110} mode, exponentially decaying with the time constant Equation 2.20. Therefore, a superheterodyne circuit is usually used for signal detection: the signal is transferred from the high-frequency region to a more convenient range for processing. The transfer is carried out using a mixer, in which a signal is generated at an intermediate frequency equal to the difference between the frequencies of the original signal and the local oscillator.

A special case of a superheterodyne circuit with a zero intermediate frequency is a synchronous detector, which outputs the TM_{110} signal envelope. The phase of the local oscillator must be stably held equal to the phase of the signal. The in-phase of the local oscillator is necessary to normalize the difference signal and to determine the initial phase of oscillations in the resonator, which makes it possible to determine the sign of the beam displacement.

The energy of the electromagnetic field is removed from the resonator by means of a pair of diametrically located whip antennas and fed to a high-frequency sum-difference device. The bandpass filter selects a part of the spectrum from the difference signal in the vicinity of the frequency of the TM_{110} mode. The resulting narrowband signal is amplified and fed to one of the mixer inputs, to the second input of which the local oscillator signal comes. The low-frequency harmonic of the signal from the mixer output is passed through a low-pass filter and digitized by an analog-to-digital converter. As a local oscillator signal, both an external generator, synchronized with the accelerating RF system, and a signal from the sum output of the sum difference device, proportional to the beam intensity, can be used.

2.2.4 Readout electronic system

Usually, the working frequency for cavity BPM as the readout electronics design depends on the availability and price of components. Hence an additional and weighty argument for picking the right frequency. There is undoubtedly a gap on the frequency scale, which can be considered widely spread due to commercial use or other purposes (TV-sat, mobile technology). Components and parts developed for these applications consequently are cheap and easy to obtain on the market. Contrarily more sophisticated design tools will be needed to develop individual circuits, where resources and care need to take in terms of reflections, shielding, etc.

In the case of using a hybrid, the two opposite signals (which have a phase shift

of 180°) are subtracted. This subtraction decreases the monopole mode's influence and doubles the dipole-modes' amplitude. By employing different cable lengths, the phase of 180° can be shifted. Consequently, phase shifters are connected before the hybrid to compensate the shift mentioned above.

In some cases, the amplitude from the rejection of dipole and monopole modes due to spatial filter is large enough to distribute this part. This scheme is less sensitive to phase drifts due to temperature shifts. If the switchable attenuator is integrated into the electronics, the dynamic range can be expanded. A band-pass filter rejects higher-order modes, and an amplifier amplifies the amplitude.

If the following electronics can not be located close to the cavity BPM, the signal has to be transferred via long cables. The transmission of high-frequency signals via cables is low. Hence down-conversion with a local oscillator (LO) is done to an intermediate/average frequency. Two frequencies are multiplied:

$$A\sin(\omega_1 t+\phi_1)\cdot B\sin(\omega_2+\phi_2)=\frac{AB}{2}[\cos((\omega_1-\omega_2)t+(\phi_1-\phi_2))- \\ -\cos((\omega_1+\omega_2)t+(\phi_1+\phi_2))] \tag{2.41}$$

The intermediate frequency can be transported with lower attenuation to the other part of the electronics. Here a second band-pass filter for the intermediate frequency is applied, followed by an amplifier. Two parallel down conversions (I-Q demodulation) are used with a reference frequency, the signal from the reference cavity, either with a matched phase (realized with the phase shifter previously) and with reference frequency shifted by 90°. This reduces the influence of beam angle α and bunch tilt Θ.

Two methods are employed for the I-Q demodulation: Homodyne and Heterodyne. The Homodyne one uses the same frequency as the dipole mode. Accordingly, the same intermediate frequency enters the conversion. This results in a zero frequency, as it is yielded from Equation 2.41, and only the amplitude information is kept. The second method uses a reference frequency, which differs from the intermediate frequency. In this case, a lower frequency provides the amplitude and phase information.

For instance, the remote-controlled attenuation switch is used only when a large dynamic range is required, or the first down conversion is used only if the I-Q demodulator is located far away from the cavity BPM. If the resolution above 1 μm is required, the I-Q demodulation is not employed[53].

2.2.5 Features of the design of cavity monitors

A resonator monitor is a narrowband device whose natural frequency is determined by the geometry of the resonator. The choice of operating frequency is determined by the specific operating conditions of the monitor. There is a general rule: the frequency ω_{110} should be sufficiently distant from the frequency of the accelerating voltage in order to avoid interference to the monitor from powerful HF devices of the accelerating system. At the same time, the frequency ω_{110} should be significantly lower than the upper limit of the frequency spectrum of the beam, otherwise the bunching parameter will have to be taken into account. This parameter is

approximately equal to unity for Gaussian beams with $\sigma_z \leq 1$ mm and frequencies below 40 GHz. In addition, the frequency ω_{110} should not be a harmonic of the bunch repetition rate in the multi-bunch regime.

For optimal suppression of in-phase modes, the natural frequency of the resonator must be high, as follows from Equation 2.36. The radius of the resonator is limited from below by the distortion of the field at the junction of the resonator with the vacuum chamber; in resonators with a small radius, the longitudinal field is not constant along the axis and the linear dependence on the transverse displacement of the beam is violated. Based on practical experience, the cavity radius should be at least three times the chamber radius. This means that it is practically impossible to make the natural frequency of the TM_{020} mode higher than the critical one without introducing perturbations into the cavity geometry.

Thus, there are the following arguments in favor of a high operating frequency: better common-mode rejection and a high signal level, and in favor of a low one - moderate cost of electronics and vacuum components and higher reliability and phase stability of the synchronous detector.

To operate in a single-shot mode, the voltage induced by the beam in the cavity must be high. Since the transit factor Equation 2.25 depends on the ratio $\xi = l/d$, the $\frac{\sin^2 \xi}{\xi}$ function should be optimized to the value $\xi_{opt} = 0.6086$ for an unperturbed resonator, disregarding the entrance / exit holes for the beam. In the multi-bunch mode, the shunt resistance must be optimized according to Equation 2.35. Since the intrinsic Q-factor of the mode is no longer included in the problem, and everything is determined by the coupling coefficient, the problem is reduced to optimization of the transit factor, in this case the optimal value of the ratio $\xi = l/d$ is $\xi_{opt} = 0.742$.[6]

Whip antennas are used as output devices at frequencies below 10 GHz, mainly due to the size of the waveguides at such frequencies. At higher frequencies, it is easier to use waveguides, which also provide better accuracy, since antennas at these frequencies are so small that it is problematic to provide the required tolerances for dimensions, angles, etc.

Strong coupling provides high signal magnitude and good cavity stability, but decreases the loaded Q factor, resulting in poorer common mode rejection and leading to field distortion in the cavity. When designing a resonator, it is important to determine the coupling coefficient for each output device and estimate the frequency shift; in calculations, perturbation theory or numerical methods are usually used.

2.3 Simulation tools

The composition of the waveguide couplers with beam pipe makes it very challenging, if not impracticably tricky and time consuming, to find analytical solutions for the cavity BPM device's electromagnetic field distribution. Therefore, computer-based field solvers are employed to solve differential equations with specific boundary conditions, in this case, for pick-up design and the interpretation of experimental results. Usually, these solvers are based on finite difference or finite element methods. With both methods, the solution's general idea is alike: first, the established geometry is covered with a mesh of small unit volumes, called cells, the corners of which are called nodes. This algorithm discretizes the computational volume, which allows

the differential equations for the electromagnetic fields, including the boundary conditions, to be transformed into matrix equations with variables corresponding to the fields at the nodes. Matrix inversion is then employed to get the field values. Two simulation packages used to determine the prototype geometry and evaluate RF properties are ANSYS HFSS [35] and CST[36]. Depending on the task, it is used the finite element method [11] or the finite integration technique [12].

The difference between finite element solvers and finite integration solvers is in the way of the matrix equations construction. The differential of a function $f(x)$ with respect to variable x is defined as

$$\frac{df(x)}{dx} = \lim_{\Delta x \to 0} \frac{f(x + \Delta x) - f(x)}{\Delta x} \tag{2.42}$$

where Δx is a change in x. Finite element methods express differential equations in the form as it represented in Equation 2.42 with Δx meaning the distance between bordering mesh nodes. Imposing the boundary conditions sets the values of some of the fields at particular nodes. The fields at each remaining node are then expressed as a linear combination of the fields at its adjacent nodes to give one equation for each unknown. These equations are combined into one matrix equation and matrix inversion is used to find the solution.

Generally, the nodes in a finite difference solver are uniformly distributed throughout the volume (i.e., Δx is constant), so a cubic mesh, for instance, the one used in CST while using wakefield simulations, is well suited. More complex-shaped mesh cells are possible by excluding the nodes at some of the cube corners to produce triangular prisms, tetrahedrons, hexahedrons. Since the solver performs better with uniformly distributed mesh cells, the whole mesh must be dense enough to cover all the curved surfaces and represent the geometry's smallest details. Since the computer memory required for both meshing algorithms: finite element and finite difference methods is related to the number of mesh cells proportionally, the result of this is that simulations become time-consuming and computationally expensive. Nevertheless, because the finite difference method is less complicated than the finite element method, a higher mesh density can be solved in simulations with the same computational resources.

In the finite element method, the fields within each mesh cell are expressed in terms of basis functions:

$$\phi^e(x) = \sum_{i=0}^{N} c_i \psi_i^e \tag{2.43}$$

where ϕ^e is a field distribution inside element e, c_i is a coefficient and ψ_i^e is one of the element's basis functions. The basis functions can have higher-order components to improve the accuracy, but this slows down the computation [18]. In all the elements, the fields are then written into a single matrix equation; the procedure is similar to the finite difference method. Nevertheless, with the finite element method, the method of defining the matrix coefficients is more complicated. The general principle of variational methods is finding solutions that drive the main function to an extremum, a minimum or maximum point. At the extremum point, the function changes slightly, with a small change to the solution so that the best accuracy is obtained. Several variational methods exist; the one that is employed is dependent

on the solver package.

The finite element method suits very well a mesh that is composed of varying cell sizes. Thus, the mesh density can be less on average than for the finite difference method, which makes up for the higher complexity of the calculation in terms of computing time. For example, CST time-domain solver uses the tetrahedral meshing technique and, because of the way the basis functions are determined, can have mesh cells with curved edges. The mesh generated by this method improves the representation of curved geometries.

Both solvers are used for solving Equation 2.2 for the resonant cavity modes. They represent the wave equation as a matrix eigenvalue problem, where each eigenvalue corresponds to a different mode wavenumber. Solving the problem for a certain number of eigenvalues returns electromagnetic fields' distributions for the same number of resonant modes, or referred to as eigenmodes. Each mode is unique in terms of its resonant frequency that corresponds to its unique eigenvalue. Knowledge of the exact field distributions and properties from electromagnetic solvers is useful for estimating the mode shunt impedance using Equation 2.17. HFSS and CST can also simulate finite conducting cavity walls and waveguide ports to give estimates for the resonant mode quality factors.

These two simulation packages can also calculate the reflections at waveguide ports with the transmission, across the simulated geometry, between them if power enters the port with a given particular frequency or a given frequency bandwidth. Like a resonant cavity, electromagnetic fields propagate down a waveguide in the form of a sum oscillating modes. Cavity modes broadband is much less than waveguide modes so that waveguides can transfer power over a broader range of frequencies. Therefore, the simulation solves the modes of the different ports of the waveguide before concluding the transfer of power between them. Because the modes are broadband, data of only one or two waveguide modes is sufficient [13].

2.4 Equivalent circuit

It might be useful to represent a cavity beam position monitor's pick-up as an electrical circuit, which is mathematically equivalent. While peculiarities of the actual problem are not readily identifiable within the complex geometry, the equivalent circuit allows to separate them into individual electrical components with associated parameters that can be easier to resolve separately. The appropriate circuit is shown in Figure 2.7. The particle beam is replaced by a current source and the mode resonance by a parallel RLC circuit. A mutual inductance replaces the waveguide coupling [14].

An RLC circuit contains a resistance R, inductance L, and capacitance C. The inductor and capacitor in an RLC circuit can store and exchange the energy at a resonant frequency f_0. Energy is dissipated in the resistance, so the internal quality factor Q_0 can be expressed in these three values R, L, and C. An RLC circuit also has an impedance Z defined as the ratio between the voltage and current in the circuit. The impedance is complex and so includes the phase difference between oscillating voltages and currents. The real part of the impedance is equal to the resistance, and the imaginary part, called the reactance, is defined by the capacitance

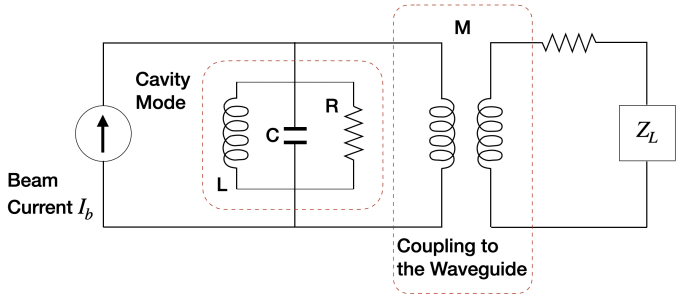

Figure 2.7. Equivalent circuit of a cavity beam position monitor pick-up.

and inductance. The impedance is given by

$$Z = R + i\left(2\pi f L - \frac{1}{2\pi f C}\right) \tag{2.44}$$

The response of an RLC circuit in time and frequency is the same as the oscillator described previously and is similar to the response of a single resonant cavity mode.

Current passing through an inductor generates a magnetic field. If there is a change in the current over time, the generated magnetic field then acts back on the inductor, which causes a potential difference across it. Two circuits may share a mutual inductance where the magnetic field in one inductor affects the potential across itself with an inductor in the other circuit. This represents how the waveguide coupling is described in the equivalent circuit [18]. A sizeable mutual inductance M lowers the external quality factor and has a small influence on the resonant RLC circuit's resonant frequency [15].

Chapter 3

6.1 GHz prototype of the cBPM

3.1 The position cavity

While designing a cavity BPM, each dimension is chosen to improve the overall system resolution and provide a simple and efficient mechanical structure. With an increase in the resonant frequency of a cavity, the entire pick-up structure's size decreases. A cavity BPM structure designed in the C-band frequency range will be compact while large enough to be machined with sufficient accuracy. Besides, high-quality components for the processing electronics are available at a lower price because of the radio communication field's advances in this frequency range [16].

With all the factors mentioned above, it was decided to design the cavity BPM in the C-Band frequency range. During the design process, after deciding the geometry and approximate values of all dimensions, the pick-up structure is simulated using electromagnetic codes to predict the performance and to optimize the overall structure [17].

Ordinarily, for the position cavity, pillbox shape is picked since it is simpler to manufacture. A cylindrical cavity was also our choice, as the resonant structure for 6.1 GHz pick-up. Equation 2.14, the radius R of a vacuum filled cylindrical cavity, corresponding to the dipole frequency of 6.1 GHz is calculated.

The resonant frequencies of the monopole, second monopole, and quadrupole modes of a pillbox cavity with a radius of 28.61 mm, calculated using Equation 2.14, will be 4.15, 7.44 and 8.2, respectively.

The amplitude of EM fields induced by a bunch in the cavity increases linearly with the cavity length. This linear increase is attenuated by the transit time factor (T_{tr} in Equation 2.25) because of the RF voltage's oscillating sine-like nature. Figure 3.1 displays the transit time factor for the monopole and dipole modes of the position cavity with different cavity length L and a constant radius of 28.61 mm. From Figure 3.1 increasing the cavity length reduces the excited monopole and dipole mode because of the transit time effect, although we can see the dipole mode decreases faster.

Compared with the dipole mode, the relative increase in the monopole mode reduces the system resolution due to the increased pollution of the monopole mode's high-frequency tail at the dipole mode frequency. Furthermore, as can be seen from Equation 2.39, the amplitudes of the signals due to the bunch trajectory and tilt also

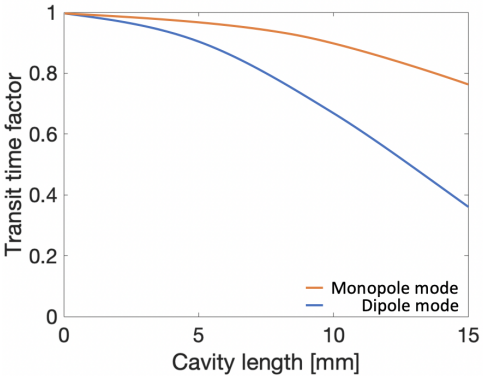

Transit time factor for the monopole and dipole modes of a pillbox cavity with different lengths.

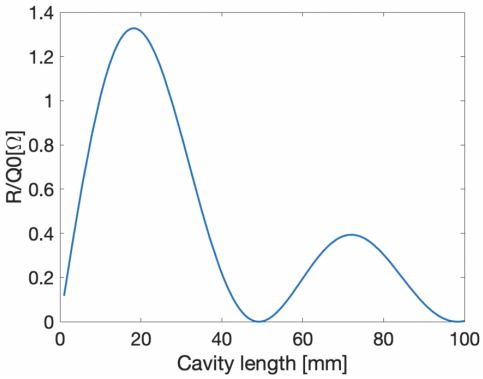

Dependence of the shunt impedance on the cavity length.

Figure 3.1. Monopole and Dipole mode Transit Time Factor with shunt impedance dependence on the cavity length [mm]

increase with the cavity longitudinal size. Considering all these factors, an initial value of the resonator length 8 mm was used for the position cavity.

From the Slater theorem, it is almost intuitive that adding a beam pipe and coupling waveguides to an isolated pillbox cavity reduces its resonant frequencies. Considering this, we took for the position cavity model with a slightly smaller radius in simulations.

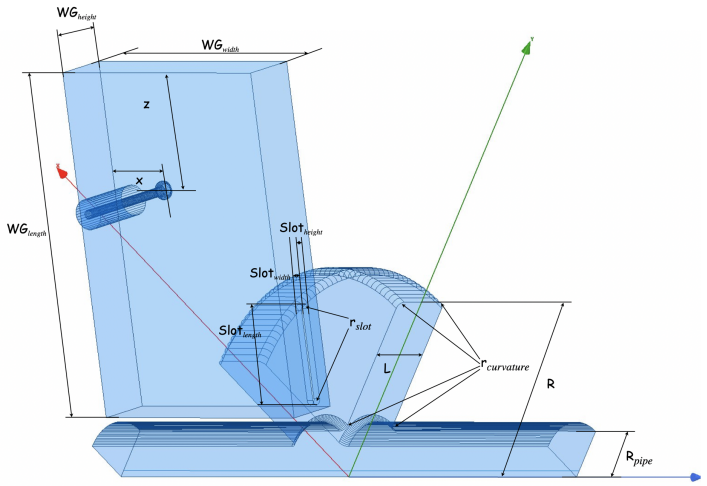

Figure 3.2. 6.1 GHz cBPM position cavity dimensions.

Forcing a symmetry boundary condition restricts the filed line's directions in the resonator. For instance, the magnetic boundary means that magnetic field lines must be perpendicular to the boundary plane. The electric boundary condition means that magnetic field lines should be parallel to the plane. Therefore, only particular modes can be excited in the structure. Reducing simulated volume in this way can save considerable simulation time while solving larger models.

The resonant frequencies of major modes were obtained using the Eigenmode

Table 3.1. Resonant Modes of The Position Cavity

Mode	Resonant Frequency/GHz		
	Analytical calculation	CST	HFSS
Monopole mode TM_{010}	4.151	4.160	4.163
Dipole mode TM_{110}	6.1	6.999	6.1002
Quadrupole mode TM_{210}	7.44	7.49	7.39

Table 3.2. Unloaded quality factor Q_0 of The Position Cavity

Mode	Q_0 value		
	Analytical calculation	CST	HFSS
Monopole mode TM_{010}	3125	3064	3173
Dipole mode TM_{110}	4076	4030	4093
Quadrupole mode TM_{210}	623	629	632

solvers in the different codes are compared in Table 3.1. The simulated values were in good agreement with the theoretical, and the difference among the codes were less than 0.05 %.

To design cBPM with relatively high quality factor, copper is the suitable material because of its higher electric conductivity of $5.97 \times 10^7 S/m$. The quality factors for the three lowest order modes simulated using Eigenmode solver of three different codes, are compared with their theoretical values in Table 3.2. The values are in good agreement with the theoretical prediction, with spread of 1.5%.

Table 3.3. Dimension values for the 6.1 GHz prototype cavity BPM position cavity.

Dimmension	Value[mm]
Position Cavity Radius R	28.61
Position Cavity Length L	8
Waveguide Length WG_{length}	33
Waveguide Width WG_{width}	48
Waveguide Height WG_{height}	8
Coaxial Position x	9.58
Coaxial Position z	17.6
Slot Length $Slot_{length}$	14
Slot Width $Slot_{width}$	1.5
Slot Height $Slot_{height}$	1
Slot Curvature Radius r_{slot}	0.75
Cavity Edge Curvatures $r_{curvature}$	0.5
Beampipe Radius R_{pipe}	7.5

The normalized shunt impedance (R/Q_0) for three modes were calculated using

Field Calculator as a post-process task on the Eigenmode simulation results. The R/Q_0 for bunch offset of 1 mm showed that the monopole mode is 97 times strongly coupled than the dipole mode, while the quadrupole is 235 times weakly coupled than the dipole mode. As the geometry is symmetric in the transverse plane, the modes' orientation was fixed by the beam offset trajectory shifted only in one plane. The cut-off frequency of the lowest transmission mode TE_{11} for the cylindrical beam pipe, which can be represented as a cylindrical waveguide, can be calculated using Equation 2.14, and it is 11.713 GHz. The two highly coupled primary resonant modes, the monopole and dipole, are well below the beam pipe's cut-off frequency. The power coupled in these modes cannot propagate through the beam pipe and decay exponentially by distance in the pipe.

3.2 Coupling of waveguide and the position cavity

Since the monitor's resolution is required to be high, the interfering signals introduced in the II chapter must be effectively suppressed. Most important is the suppression/rejection of strong monopole mode signals [24].

Particularly, these are the basic, first, and second monopole mode signals. The second monopole mode frequency is closer to the dipole mode. Two possible connection methods between the waveguide and the position cavity were studied to successfully decouple monopole modes while maintaining sufficient coupling to the dipole mode. Below we will discuss the advantages and particular reasons when to use which one. A similar method is used for the damping of higher modes in the acceleration structures [25].

The full structure of a position cavity in the cBPM contains a cylindrical resonator and four waveguide adapters connected to it Figure 3.2. A rectangular or semi-rectangular slot is cut out in the pillbox cavity wall Figure 3.3.

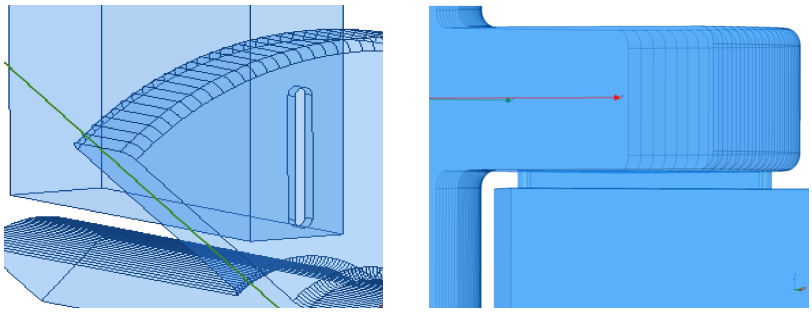

Figure 3.3. Slot coupled waveguide, schematic view.

The coupling slot's length is parallel to the plane where the dipole mode satisfies an electrical boundary condition [53]. The slot disrupts the currents flowing in the resonator walls. Hence, The coupling between the dipole mode TM_{110} of the cavity and waveguide is very sensitive to the slot's longitudinal dimension; therefore, coupling improves between cavity and waveguide adapter if the aperture of slot starts near the electromagnetic center of the cavity. In this way, the dipole mode generates an electromagnetic field in the slot that looks like half the TE_{01} wave in the rectangular waveguide. The slot is widened with gaps in the resonator walls,

through which the induced dipole mode field continues into the coupling waveguide as a TE_{01} wave.

Because of their symmetry, the monopole modes can only form a field in the slot that corresponds to the higher TE_{110} mode of the waveguide. This wave's cut-off frequency is higher than that of the TE_{01} wave, especially if the slot is narrow; coupling between the fundamental mode and waveguide adapter is sensitive to the transverse dimension of the slot. So a resonator structure can be constructed where the low monopole modes cannot propagate into the waveguide.

On the other hand, since slot cut-off frequency is higher even than dipole mode frequency, one should try to keep the coupling slot height low enough to avoid attenuation of the signal proportional to the beam offset. While using a coupling slot, the waveguide cut-off frequency is usually chosen to be below the dipole mode frequency [26].

Because of the limited mechanical accuracy in the resonator's construction, the plane of symmetry of the slot is slightly shifted from the plane of symmetry of the resonator. Therefore, monopole modes can still propagate in the waveguide as a TE_{01} wave. Although the coupling is low, the monopole modes' output can be comparable to the dipole mode signal. Therefore, the mechanical tolerances must be kept small.

When waveguides are connected to the cavity directly, to decrease the coupling of fundamental mode to the waveguide, the waveguide aperture width should be kept small.

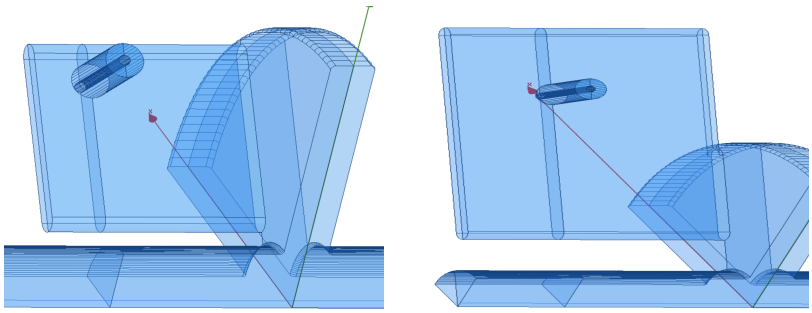

Figure 3.4. Directly coupled waveguide, schematic view.

After the waveguide dimensions are determined according to the requirements and the optimal conditions, the waveguide's cutoff frequency for the lowest TE_{01} wave is higher than the resonance frequency of the fundamental mode. It is located between the monopole and dipole mode frequencies of the position cavity. In this way, the part of the remaining fundamental mode signal, which is lower than the cutoff frequency, is subsequently suppressed in the waveguide.

In order to determine the tolerances of the resonator dimensions, the deviations in the resonance frequency were estimated with HFSS Table 3.4. For this purpose, the resonance frequencies for the changed dimensions were calculated. In doing so, fairly large changes comparable to the grid step size were expected. Then the results were approximated for a change of $1mm$.

The results of this simulation show that tolerance of tens of μm is sufficient for all dimensions except for the radius and coaxial port-related values. For the

Table 3.4. Dimension tolerances to the 1mm change for the 6.1 GHz prototype cavity BPM position cavity.

Dimmension	Q_0 Variation [%/mm]	Frequency shift [MHz/mm]
Cavity Radius R	2	-270
Cavity Length L	11	-21
Waveguide Length WG_{length}	11.5	-0.1
Waveguide Width WG_{width}	4.2	-0.6
Waveguide Height WG_{height}	6	-0.4
Spacing s	12.3	0.2
Slot Length $Slot_{length}$	19.2	5.2
Slot Length $Slot_{height}$	24.3	493

Table 3.5. The main characteristics of the 6.1 GHz prototype cavity BPM position cavity.

Parameter	Numerical calculation
	TM_{110}
f_{GHz}	6.100
Q_0	4076
Q_L	1019
Damping time,τ ns	53.2
$\frac{R}{Q}$,Ohm	0.52
V_{out}	2.3 $V/nC/mm$

radius to which the frequency reacts very sensitively, the tolerance must not exceed $10\mu m$. The analytically and numerically calculated resonance frequencies, shunt impedances, and monitor signals for the prototype can be seen in Table 4.2. The resonance frequency of the dipole mode calculated analytically for the numerically optimized resonator dimensions using the approach differs from the analytically obtained value by more than 5%, because the frequency is calculated analytically for a closed resonator without slots and waveguides. The analytically and numerically calculated resonance frequencies of the fundamental mode correspond to one another very well because the influence of the slot on the resonance frequency of the monopole mode is small. If the dipole mode's shunt impedance is known, the output signal can be estimated with the formula Equation 2.30.

An estimate of the thermal noise based on a bandpass filter's assumption with a bandwidth of $100MHz$ results in a noise voltage of $9\mu V$. Therefore, the signal level is much higher than the noise level, i.e., theoretically, a resolution better than $100nm$ can be achieved. EM simulations estimated the monopole mode's influence on a structure where the slot is shifted from the symmetry plane of the resonator.

The portion of the fundamental mode signal that lies outside the dipole mode's frequency range is also suppressed by a bandpass filter in the receiver electronics at around 80 dB. The frequency selective decoupling devices carry out subsequent suppression. The portion of the fundamental mode signal at the dipole mode

frequency is 60 dB weaker than that in resonance. The influence of the monopole mode is then negligibly small.

3.3 Waveguide to coaxial transmission

In the previous section, the coupling, as the loaded quality factor, could be determined by the waveguide dimensions or slot aperture area with the pillbox cavity. Now we are loading waveguides with the coaxial feed-throughs. The induced signal is extracted from the resonator via waveguides that are coupled to the coaxial loads with matched impedance. Depending on the position of the load on the waveguide, several parameters are changed dramatically. The position of the coaxial coupler changes the quality factor, amplitude of the signal which is extracted from the cavity; in other words, if we imagine a system where excitation comes from one end of the short-circuited waveguide and is extracted from the coaxial coupler, the ultimate goal is to reach lowest S_{11}, reflection coefficient, and highest S_{12}, transition coefficient.

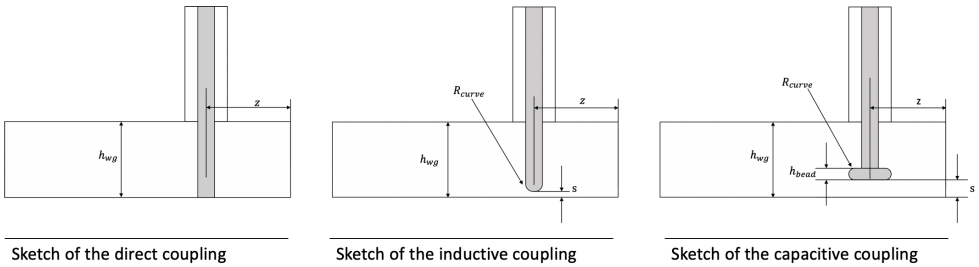

Figure 3.5. Differnet types of coupling simulated for better waveguide to coaxial matching.

The waveguide dimensions can be chosen such that it restricts the monopole from coupling into the waveguide (as explained in the previous section). shows the simulation model of a waveguide adapter with the matched coaxial coupler, along with the dimensions and ports. According the width w_{WG} of a rectangular waveguide, given the cutoff frequency $f_{cut}$of TE_{01} is, $w = \frac{c}{2}\left(\frac{1}{f_{cut}}\right)$, where c is the speed of light. The guide-wavelength, inside the waveguide, corresponding to the cavity dipole mode frequency can be calculated as [7],

$$\lambda_{g,110} = \frac{\lambda_{g,110}}{\sqrt{1 - \left(\frac{\lambda_{110}}{\lambda_c}\right)^2}} \tag{3.1}$$

where λ_{110} is the free space wavelength for the dipole frequency and λ_c is the cutoff wavelength of the waveguide mode, which is twice the waveguide width ($2w_{WG}$) for the TE_{01} mode of a rectangular waveguide. The interpretation of the position signal becomes complicated if the waveguide also resonates at the cavity's dipole frequency. To avoid matching the waveguide's resonances to the position cavity's, the waveguide's length should not be an integer multiple of the half guided wavelength $\lambda_{g,110}/2$. The field, coupled into the waveguide from the monopole mode, will decay exponentially.

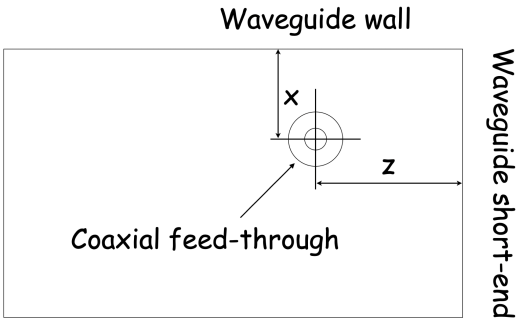

Figure 3.6. exposition of how sufficient transition is achieved between the waveguide and coaxial antenna by changing the x and z parameters.

The quality of transmission is susceptible to geometrical dimensions itself. One has to remember that when the operating frequency is high, the size of the structure itself is getting small, which makes coupling between the coaxial load and waveguide difficult. The transition depends not only on the position of the load but also on the geometrical shape of the coupler's inner conductor. The coupler's overall dimensions become very limited in terms of size when there is reduced volume, in case of high frequencies. We have simulated three different mechanical solutions for transmission design .

Three different coupling methods were studied, using the whip antenna for inductive coupling. Preforming capacitive coupling, whip antenna with a flat bead at the end of the inner conductor, and mounting coaxial antenna to waveguide wall directly. In the capacitive coupling case, we have a little more freedom in terms of distance from the waveguide wall, Since the capacitance between two flat surfaces is proportional to their area and inversely proportional to their separation. Increasing the area of the bead should allow for a larger spacing between it and the waveguide wall.

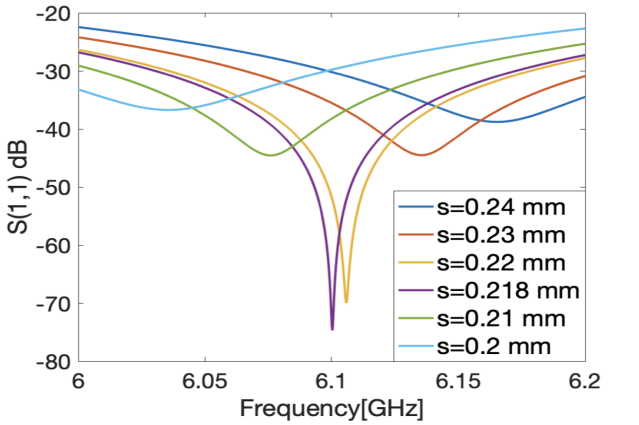

Figure 3.7. S_{11} parameter dependence on the spacing variation between the whip antenna end and waveguide wall.

To evaluate how sensitive the waveguide to the coaxial transmission line is towards the spacing of the inner conductor of coaxial feed-through and waveguide, the first system to study through simulations was transmission with whip antenna Figure 3.7.

The S(1,1) parameter minimum changed dramatically according to changing the spacing s only by 0.01 mm in the whip antenna case. The minimum appeared at a different frequency; also, the minimum range level rose from -70 dB− -80 dB to the -30 dB− -40 dB. Demanding the 0.01 mm scale precision is already a very mechanically advanced requirement if not impossible; the latter depends on the device's part.

The capacitance coupling was simulated to maintain a low level for dB S(1,1) parameter despite the possible manufacturing errors. The whole system was more stable to spacing s errors and even less sensitive to the coaxial position errors. If 0.01 mm error of s rose S(1,1) [dB] up to the -50 dB− -40 dB, for position error 0.02 mm it remains in -60 dB− -50 dB interval Figure 3.8.

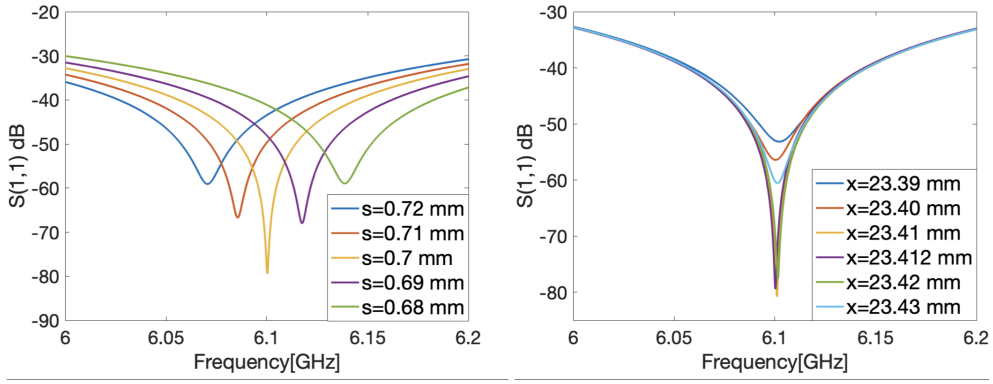

dB S(1,1) parameter dependence on the spacing between the bead and waveguide wall.

dB S(1,1) parameter dependence on the distance between the antenna center and waveguide wall.

Figure 3.8. S_{11} parameter dependence on the spacing and position variation of the coaxial feedthrough.

The resonances that are part of the resonance antenna couplings are simulated along with the cavity modes. These resonances couple magnetically to the cavity dipole mode at the point where the waveguide is connected to the cavity. This can be represented as two magnetically coupled resonant electric circuits made from passive components, as discussed in the equivalent circuit section. The effective impedance Z_{eff} of a circuit representing the cavity is given by

$$Z_{eff} = Z_c + \frac{(2\pi f)^2 M^2}{Z_a} = Z_c + \frac{(2\pi f)^2 M^2}{|Z_a|^2} Z_a^* \tag{3.2}$$

where f is the operating frequency, M is the mutual inductance, and Z_c and Z_a are the impedances of the uncoupled cavity and antenna circuits respectively [15]. The second term on the right-hand side of Equation 3.2 is the reflected impedance, and it is proportional to the complex conjugate of the antenna circuit impedance. In other words, if the driving frequency f is below the resonance of the antenna circuit, the reflected impedance is capacitive and increases the resonant frequency of the

Table 3.6. Dimension values for the inductive and capacitive couplings for 6.1 GHz.

Dimmension	Value[mm]	
	Inductive coupling	Capacitive coupling
Waveguide Length l_{WG}	33	33
Waveguide Width w_{WG}	48	48
Waveguide Height h_{WG}	8	8
Coaxial Position x	9.63	23.41(2)
Coaxial Position z	9.63	17.3
Beahd Height h_{bead}	–	1.2
Antenna Curvature Radius R_{curve}	0.5	0.5
Whip and Bead Radius	0.635	1.3
Spacing between Antenna and Waveguide Wall s	0.21(8)	0.7

cavity circuit. On the other way, if the frequency is higher than the antenna circuit resonance, the reflected impedance, in this case, is inductive, and it decreases the resonant frequency of the cavity circuit. If the driving frequency is far enough from the antenna circuit resonance, the imaginary part of the antenna circuit impedance, which is the reactance, becomes greater than the real part, the resistance, and the imaginary part of the reflected impedance is reduced.

Consequently, the results can be translated in the following way in case of a waveguide and coaxial coupler in cBPM environment. The measured resonant frequency is the resonant frequency of the system, which is already coupled. As the gap between the end of the coaxial antenna and the wall of the waveguide is increased, the frequency of the antenna resonance is also increased. In the case of small spacing, the frequency of the antenna resonance is below the position cavity's dipole mode frequency, and hence the measured resonant frequency is pushed up, as when the reflected impedance is capacitive. As the separation is enlarged, the antenna resonance passes the resonant frequency of the cavity TM_{110} mode and begins to push the measured resonant frequency down, as when the reflected impedance is inductive. As the frequency of the antenna resonance is increased further, its reactance at the frequency of the cavity dipole mode becomes high enough, so that the reflected impedance is reduced. At this time, the measured resonant frequency reaches a minimum and then begins to return to the frequency of the uncoupled cavity dipole mode. In the cBPM system, the antenna also has the function of matching the impedance of the waveguide to the $50\,\Omega$ impedance of the coaxial output. For that reason, the maximum output, S_{21} parameter, is not certainly seen when the antenna is resonating with the cavity dipole mode, since there is a chance that power may be reflected back into the waveguide. For the best performance, the waveguide should be designed so that the antenna resonance and the minimum reflection, S_{11}, should appear at the frequency of the position cavity dipole mode.

3.4 Study of possible manufacturing errors by EM simulations

The cBPM will be fabricated with low tolerances in sensitive areas such as the pillbox cavity radius. Even with the specified tolerances, the resonant frequencies of the dipole modes can vary by several MHz from the simulated resonant frequencies. The possible errors in fabrication that can change the cavity parameters are studied using simulation.

The coupling and isolation between the ports should be the most sensitive to the coupling slots' position errors. With copper as a cavity material, the present computer numerical control machines can machine and measure geometry with accuracy well of the order of several 10 of μm. As the cavity is fabricated with tolerances below 100 μm, it can be set as the upper limit for machining critical parts' errors. Different scenarios were simulated with different fabrication errors, and their effects on the cavity parameters were studied.

3.4.1 Coupling slot shift

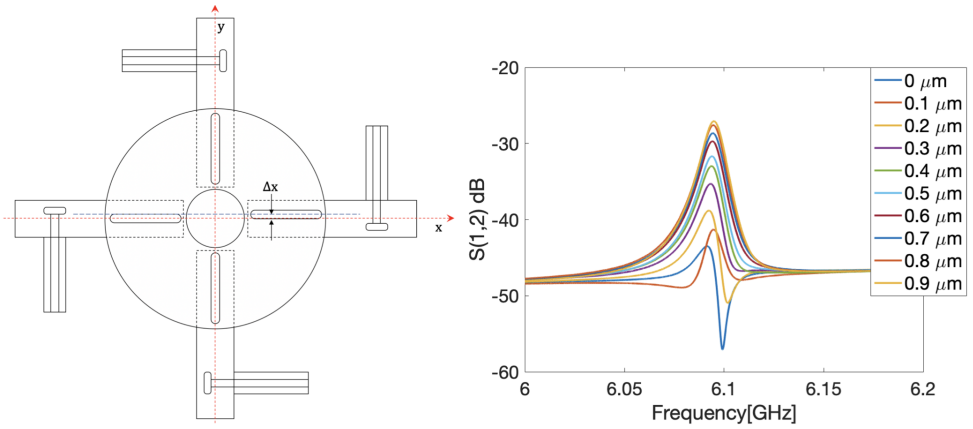

Sketch representing simulation model for simulated S-parameters of a cBPM prototype with the slot shifted from its original position.

Simulated S-parameters of a cBPM prototype to study the effects of the slot shifted from its original position offset by 0-0.9 mm along perpendicular axis.

Figure 3.9. Sketch representing simulation model for simulated S-parameters of a cBPM model with the slot shifted from its original position with simulation results.

If the slots are shifted towards either side of the axes, the magnetic field from the orthogonal dipole mode should cross-couple into the slots and decrease the x-y isolation.Figure 3.9 represents a sketch of a cavity BPM with one of its slots shifted by a small amount Δx from the x-axis. All other dimensions were left the unchanged. The cBPM geometry with one slot shifted by different position offsets Δx were simulated using HFSS in the dipole frequency region. The S-parameters were generated. The ports and boundary conditions were assigned similar to the model of the ideal geometry.

The left part of Figure 3.9, shows the S-parameters for a cBPM with slots shifted

from 0 to 0.9 mm. When the slot was shifted along the y-axis, the trace S_{12} examined the case where the slot along the x-axis was shifted towards the slot along y-axis positive direction. The slot was shifted over 0 to 0.9 mm in several steps. For slots offset by 0.9 mm, the isolation degraded up to 26 dB, which was without shift error on the order of 45 dB observed during S-parameter simulations. The possible manufacturing errors due to slot shift alone did not alter the cavity parameters by the amounts observed from the RF measurements.

3.4.2 Coupling slot rotation

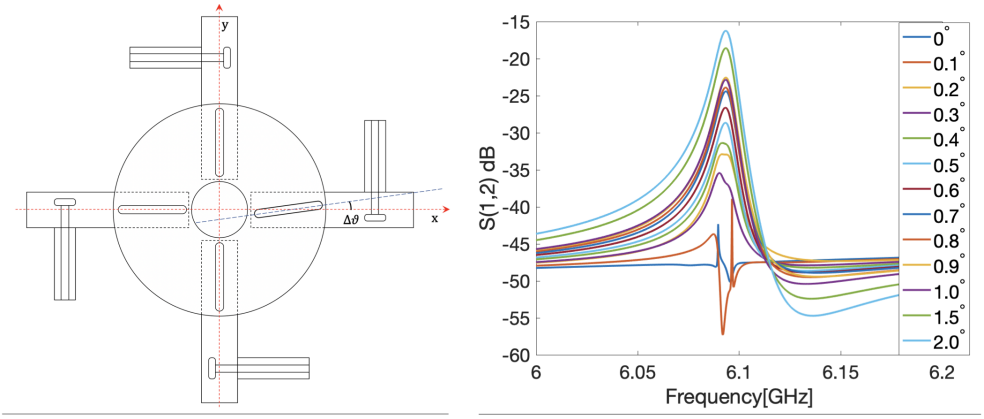

Sketch of a cBPM model used to study the S-parameters of a prototype design with slot rotated by Δθ.

S-parameters of a cBPM with slot rotated by 0°-2°.

Figure 3.10. Sketch of a cBPM model used to study the S-parameters of a prototype design with slot rotated by $\Delta\theta$

Similar to shifted slots, another possibility can be that the slots are rotated around the cavity center (z-axis). If there is no perfect alignment between the slots to the x or y axes, the axial symmetry is broken, which changes the resonance modes' orientation. Due to the field's rotation, the cross-coupled magnetic field from the orthogonal dipole mode increases, reducing the orthogonal port's isolation.

An example sketch of a simulated model of cBPM, representing the slot rotation around the z-axis, that has been rotated by an angle $\Delta\theta$, is displayed in Figure 3.10.

The two orthogonal slots, located along the y-axis, and one aligned on the x-axis, were kept in the same position. Different angles rotated the slot up to 2°, and the transmission of orthogonal port characteristics of the cBPM were simulated using HFSS. The S-parameters calculated for the slot rotation from 0-2° are plotted on the left side of Figure 3.10. The x-y isolation reduces to 22.87 dB when slots rotate by 1° and further up to 16.24 dB for the rotation of 2° . This simulation replicates a scenario in which a cBPM would have been moved after milling two of the four slots and then relocated to cut the remaining two.

The variations in the simulated resonance frequencies and transmission attenuation were not large enough to compromise RF desgin. Based on the simulations, the slot rotation should neither lower the resonance frequencies nor degrade the x-y

isolation dramatically.

3.5 6.1 and 4.15 GHz prototype cBPM

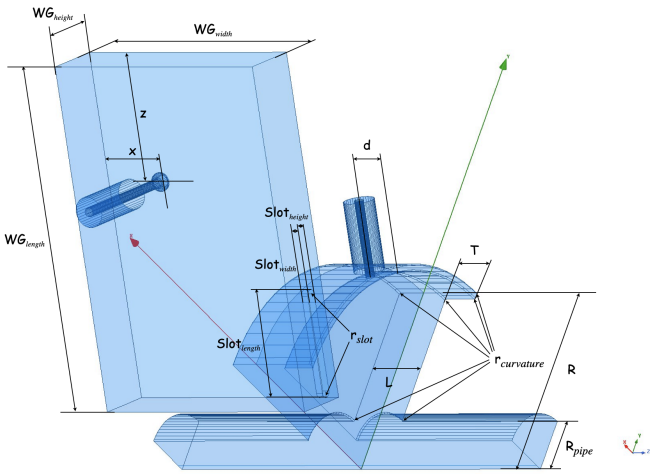

Figure 3.11. A general sketch and indications of the dimenions for the cBPM prototype used in simulations with dipole mode 6,.1 GHz and monopole 4.15 GHz

The same cylindrical resonator is used to obtain the signals from both dipole 6.1 GHz and monopole 4.15 GHz modes excited by the beam. Such a mechanical decision makes the BPM more compact for placing it in the EuPRAXIA project. To measure a single bunch trajectory within 30 ns timescale, we used the same capacitance coupling as in two resonators prototype and slot longitudinal size to adjust cavity Q-factor. Below is presented a BPM detailed numerical study and analyze its tolerance requirements for submicron resolution.

The proposed EuPRAXIA project requires very precise control of the beam parameters by employing high-resolution beam instruments. The project needs cBPMs with < 1 μm resolution. A C-Band cavity BPM is being developed at LNF INFN in order to meet these requirements. The design is based on TM110 dipole selective mode coupling. Since we are limited in available space, a different feature to BPM design was implemented in simulations. The difference is the conception of one joint cavity as both monopole and dipole signal sources. Using a joint cavity allows saving double longitudinal space.

The proposed microwave cBPM consists of the simple cylindrical cavity exited in the TM110 mode by a shifted beam from the central axis. A general sketch of the cBPM prototype is displayed in Figure 3.11.

The cavity is loaded with coupling ports. Four slots utilize magnetic coupling with dipole modes and extract beam position signals in two orthogonal planes. Another four SMA-type coaxial feedthrough is connected to the resonator and provide monopole signal to determine a bunch charge. The copper material was chosen for cavity production to minimize possible thermal losses and to have higher quality factor. The prototype design parameters of the cBPM are given in the Table 3.7.

Table 3.7. Dimension values for the one resonator prototype cavity BPM

Dimmension	Value[mm]
Position Cavity Radius R	27.71
Position Cavity Length L	8
Waveguide Length WG_{length}	33
Waveguide Width WG_{width}	48
Waveguide Height WG_{height}	8
Coaxial Position x	9.58
Coaxial Position z	17.6
Separation of Monopole Coaxial Port d	2.4
Trench Length T	5
Trench Height h	1
Slot Length $Slot_{length}$	14
Slot Width $Slot_{width}$	1.5
Slot Height $Slot_{height}$	1
Slot Curvature Radius r_{slot}	0.75
Cavity Edge Curvatures $r_{curvature}$	0.2
Beampipe Radius R_{pipe}	7.5

In order to increase dipole mode coupling, since slot size is limited by cavity radius, approache was the idea of capacitance coupling. The waveguide to coaxial transition forms itself low-Q resonator with highest S_{12} parameter at the cavity dipole mode frequency. It helps to enhance the overall coupling coefficient.

The coupling slots perturb the theoretical field distribution. That breaks the dipole mode cosine azimuth dependence and causes the pseudo-quadrupole components occurrence.

Manufacturing errors may cause the significant degradation of cBPM overall performance. The primary reasons are resonant frequencies shift, common-mode leakage to the coaxial port, and orthogonality breaking between two dipole mode polarization. The cavity resonant frequency shifts will be problematic for further signal processing since the difference between dipole and monopole frequencies should be constant. The monopole mode coupling results in the blind spot near the cBPM electrical center, for small offsets, in other words, and therefore limits the prototype's resolution. The dipole mode's nonorthogonality induces cross-coupling between x-y coaxial ports. While the symmetrical loaded x-y coupling can be removed numerically, the general irregular reflections from electronics and feed-throughs may also degenerate the cBPM dynamic range. We take into account three possible fabricating errors as displayed in Figure 3.12 to evaluate their influence on the cBPM performance. As displayed, there is no signal attenuation between opposite ports for simulated possible fabricating errors. It is also possible to maintain - 40 dB isolation between the orthogonal ports while allowing reasonable mechanical tolerances.

Misalignments due to the fabrication errors result in non-zero projections of the magnetic field components of the TM_{010} mode in the coupling slot, produces monopole mode coupling to the waveguide. The results are displayed in Figure 3.13. It appears, that the monopole mode coupling is most sensitive to the slot rotation

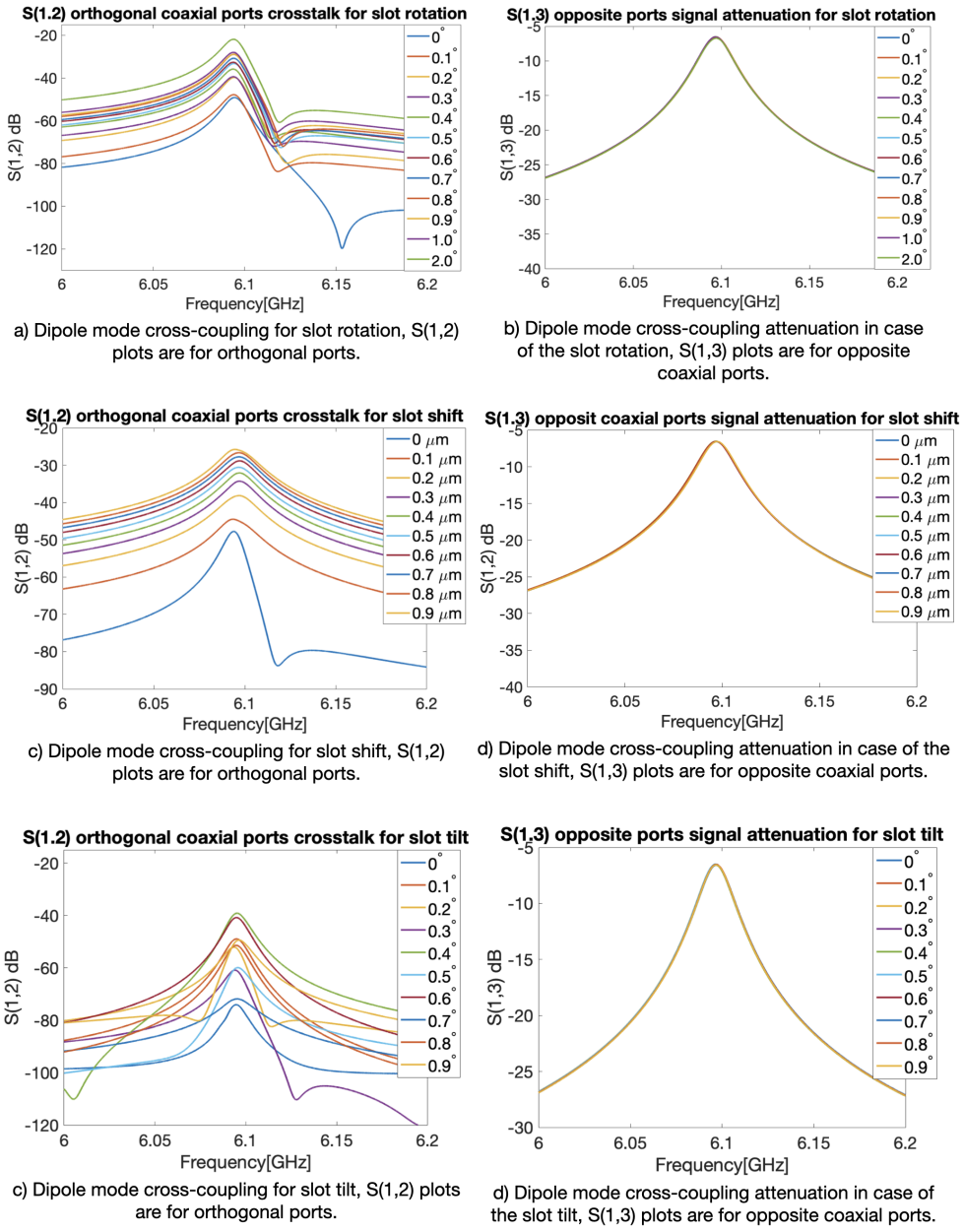

Figure 3.12. The x-y port cross coupling for coupling slot rotation, shift and tilt

misalignment.

In General, increasing the coupling slot length increases the voltage amplitude excited by the dipole mode. However, to maintain the decay time τ around 30 ns, we tried to compromise between the quality factor and output voltage depending on the coupling slot length Figure 3.14.

Loading with four coaxial feed-throughs a single resonator is not convenient since they couple, not only with the monopole mode but also with the dipole. Thus, decreasing the quality factor of the most crucial magnetic mode. One also has to remember that two dipole mode polarisations are coupled out from the cavity and

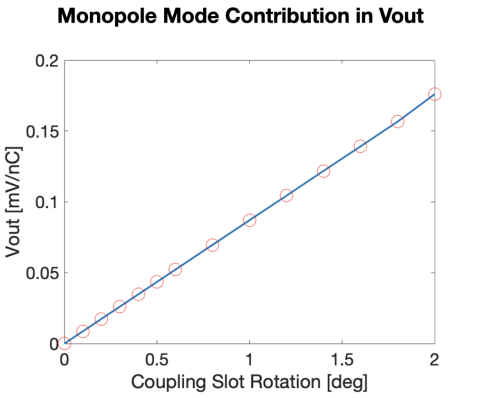

Monopole mode leakage result in terms of its contribution in Vout at coaxial port for coupling slot rotation

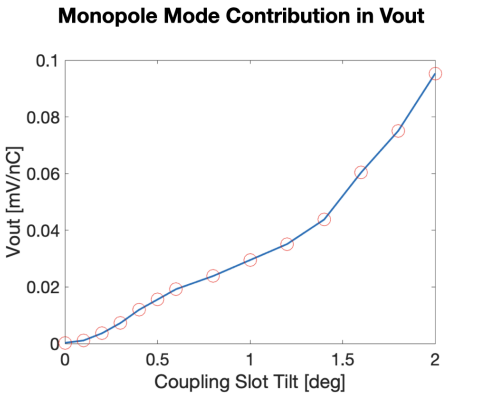

Monopole mode leakage result in terms of its contribution in Vout at coaxial port for coupling slot tilt

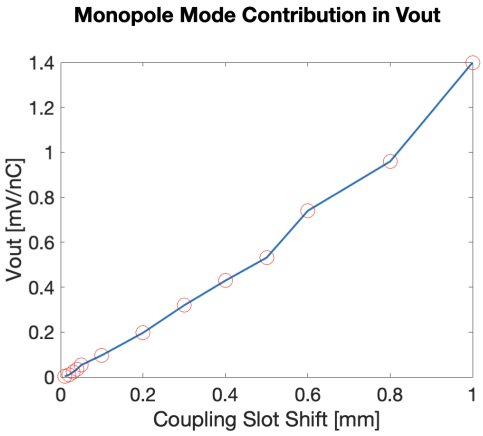

Monopole mode leakage result in terms of its contribution in Vout at coaxial port for coupling slot shift

Figure 3.13. Monopole mode leakage due to the fabricating errors, such as coupling slot shift, tilt and rotation

are translated into the beam offset in each plane, x, and y. To get a high enough quality factor for dipole mode and not decrease the coupling to waveguides, it was considered to use only two coaxial ports, having 50Ω impedance, and the other two to not break the spatial symmetry.

Hence, we get two orthogonal coaxial ports with 50Ω to extract the monopole mode and four waveguides to couple out the dipole mode.

The quality factor of the dipole mode increased from 1756 to 3075 with coupling constant β to waveguides equal to 2.6.

One resonator cBPM, definitely has some advantages, especially when the longitudinal space is a critical factor, but it also needs precise manufacturing. Especially in this particular layout, it is tough to maintain high loaded quality factor for monopole mode. The higher is the resonant frequency, the smaller the separating distance d should be to decrease coupling.

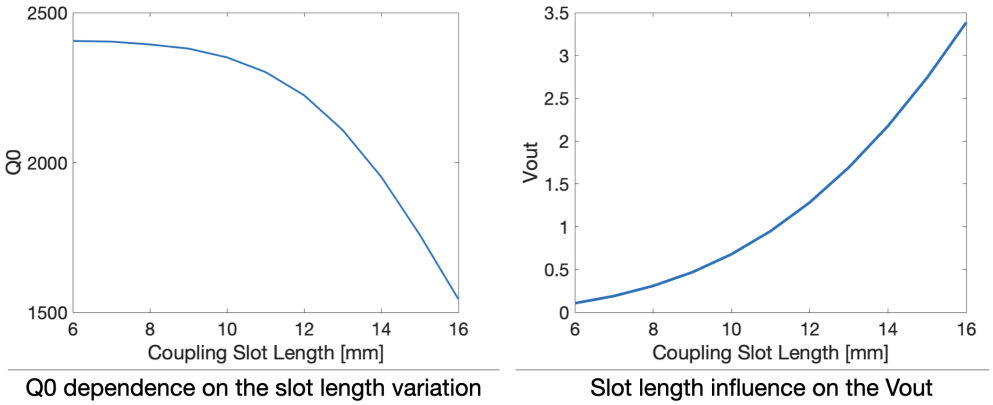

Figure 3.14. Coupling slot influence on the internal quality factor and output voltage for dipole mode

Table 3.8. Dimension tolerances to the 1mm change for the one resonator prototype.

Dimmension	Q_0 Variation [%/mm]	Frequency shift [MHz/mm]
Cavity Radius R	2	-218
Cavity Length L	3	-33.9
Waveguide Length WG_{length}	-2.3	-0.2
Waveguide Width WG_{width}	-3.81	-0.3
Waveguide Height WG_{height}	-6.93	-0.6
Separation Coaxial Port d	20	1.6
Spacing s	8	0.1

Table 3.9. The main characteristics of the one resonator cBPM prototype

Parameter		Numerical calculation
	TM_{010} as reference	TM_{110}
f_{GHz}	4.18	6.100
Q_0	2631	3075
Q_L	657	877
Damping time,τ ns	34.3	44.5
$\frac{R}{Q}$,Ohm	42	0.49
V_{out}	21 V/nC	3.02 $V/nC/mm$
Theoretical resolution	–	26 nm

When this design was prepared, the longitudinal size of cBPM was one of the crucial parameters. Due to this, we started studying cBPM design with only one cavity. Single cavity BPM needs a more complicated and expensive read-out electronic system and more tight mechanical constraints. Indeed, such devices will exploit two different modes of the same cavity that must have a fixed frequency difference; tuning such difference can be extremely difficult and impractical. It was

decided to mention it in a thesis as a possible solution, especially when longitudinal size is critical. Even though the RF design provides the same order of magnitude output voltage for dipole mode, treating the signal gets very complicated from the read-out electronics point of view.

Chapter 4

5.1 GHz prototype of the cBPM

Even though the 6.1 GHz monitor meets the requirements for use in the EuPRAXIA, after interaction with the electronic group, the design frequency was moved down to 5.1 GHz to reduce possible interference with the X-band Linac operating frequency. Also, it is a mechanically advanced device from the design point of view. The complex layout of the 6.1 GHz prototype complicates its precise manufacturing as its vacuum construction. For these reasons, a monitor for 5.1 GHz was developed. That is larger and less sensitive to mechanical errors due to the modified layout than the 6.1 GHz monitor. The RF components for the receiver electronics are cheaper than those for 6.1 GHz.

This chapter describes the design and Electromagnetic simulation verification of the prototype with dipole mode frequency 5.1 GHz.

4.1 Design of the 5.1 GHz prototype

Some changes have followed the difference in the resonance frequency of the monitor in its construction. In the first approach, the 6.1 GHz prototype's conceptual design was replicated with minor changes, excluding the changes that are directly dependent on the working frequency of the monitor, such as cavity radius or wvaguides cut-off frequency. As an example of these minor changes, one can consider, for instance, the waveguide height, which was 8 mm in the 6.1 GHz case, and for the 5.1 GHz 6 mm, is used.

Consequently, with the waveguide dimension change, a new optimized position must be determined for the coaxial coupler Table 4.1. Further simulations were performed in order to find ways to decrease the sensitivity to the spacing between the coaxial antenna and waveguide wall. Increasing the area of the coaxial end should therefore allow larger spacing between it and the wall of the waveguide. To do so, the radius of the bead was increased from 1.3 to 1.8 with the curvature radius of the attached circular bead edge decreased from 0.5 mm to 0.2 mm; thus, providing a larger plane area at the end of the antenna.

The 6.1 GHz design of the transition between the waveguide and the coaxial using the capacitance antenna coupling was based on simulations of the end of the waveguide including the transition. Two ports are defined, the open end of the waveguide and the cross section of the coaxial antenna, and the simulation results

Table 4.1. Coaxial coupler and waveguide transition line parameters Figure 3.3

Dimmension	Value/mm		
	Direct coupling	Inductive coupling	Capacitive coupling
Whip Antenna Raduis	0.635	0.635	0.635
Bead Radius	–	–	1.8
Bead Height h_{bead}	–	–	1.2
Curvature Radius R_{curve}	–	0.5	0.2
Spacing s	0	0.151	1.969
Distance from the short-end$z$	19.5	58.8	21.74
Distance from the wall x	25	18.5	12.2
Waveguide height h_{wg}	3	8	6
Waveguide height w_{wg}	39	37	37
Waveguide height l_{wg}	57	90	57

the port S-parameters. An improvement on the design of the antenna was attempted using the S-parameter simulation tool, which is part of the [35] package.

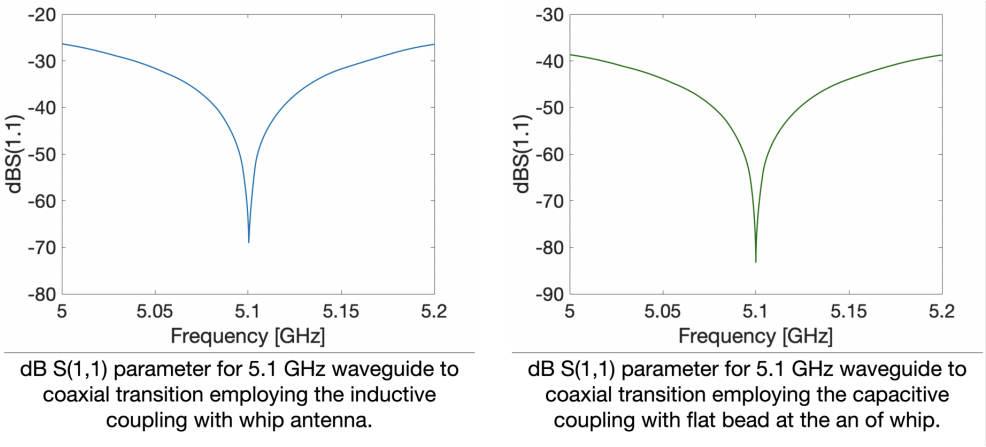

Figure 4.1. dB S(1,1) parameter for inductive and capacitive couplings for 5.1 GHz waveguide to coaxial feed-through transition line.

One might notice, that these minor change in the coaxial coupler geometry provides the additional -5dB when measuring the S(1,1) parameter, which can be observed on the Figure 4.1. Similar features appear in other BPM designs [20],[18].

In general, a larger bead radius loosens the tolerance towards the spacing dimension s; thus, a suggestion could arise to increase the bead radius further, but it was decided to keep the coaxial coupler extraction point simple and keep the SMA connector dimensions.

Although using coupling slots to connect the waveguide and the position cavity provides sufficient rejection of fundamental mode and good isolation between the orthogonal ports, it also doubles the possibilities of manufacturing errors. As slots could be misaligned as to the cavity as to waveguides. Hence, the slots that couple the position resonator and waveguides in the 6.1 GHz structure are removed in the 5.1 GHz structure to simplify the overall design. Waveguides are connected to the

position cavity directly, instead. Rectangular waveguides are used for coupling.

These changes in the design suggest several modifications that have to be also made. First, since the waveguides are directly coupled to the position cavity, to effectively decouple the monopole mode and keep sufficient isolation between the orthogonal ports, waveguide height should be relatively small, 2-4 mm instead of 6-8 mm. This dimension, of course, depends on the working frequency.

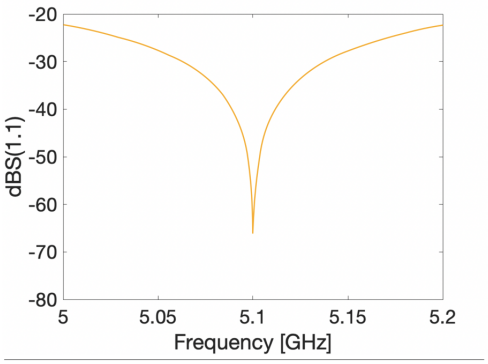

dB S(1,1) parameter for 5.1 GHz waveguide to coaxial transition employing the direct coupling with whip antenna.

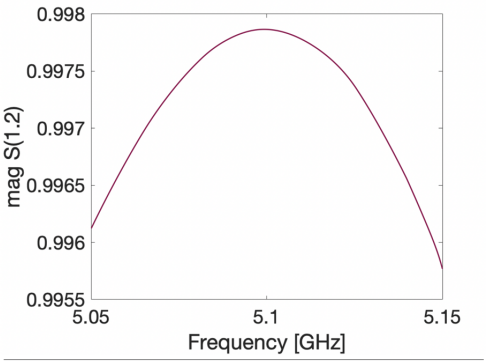

Mag S(1,2) parameter for 5.1 GHz waveguide to coaxial transition employing the direct coupling with whip antenna.

Figure 4.2. dB S(1,1) paramter for direct coupling with | S(1,2)| paramter plot.

Since there is reduced volume in the waveguide after changing its height, it will be much more convenient to use direct coupling than capacitive.

Corresponding plots for S(1,1) [dB] and the magnitude of S(1,2) parameter are displayed in the following graphs Figure 4.2. As it can be observed, the results are comparable with the capacitive coupling case. Here, dimensions are kept as they are for the SMA connector, the inner conductor radius is 0.635 mm, and for the outer radius, it is 2.125 mm.

Different positionings and layout for waveguides coupled to the position cavity were simulated to determine the composition, where the immense amount of signal of induced dipole mode transmits and couples out from the feed-throughs. Figure 4.3

In Figure 4.3 above mentioned waveguide to the coaxial transmission for direct coupling is employed; the difference between them is the filed propagation direction in the waveguides. As it is displayed, the |S(1,3)| is around 16-20. The result is slightly better when the field coupled out from the cavity propagates parallel to the position cavity, not perpendicularly.

In Figure 4.4, simple rectangular waveguides are used. The difference is in waveguide heights, it is 3mm and 2mm respectively. The waveguides are not connected to the beam pipe as in [56] or [23]. The |S(1,3)| paramter in this case varrys from 39 to 47.

Even though coupling between the waveguide and resonator is better with connected waveguides to the beampipe, it decreases the loaded quality factor Q_L. On the one hand, one could fix this issue by placing the coaxial coupler closer to the waveguide wall; however, this decreases the output voltage for dipole mode V_{out}.

In order to estimate the amount of the signal transferred from the position cavity and coupled out with coaxial ports, the measurement method based on a coaxial wire

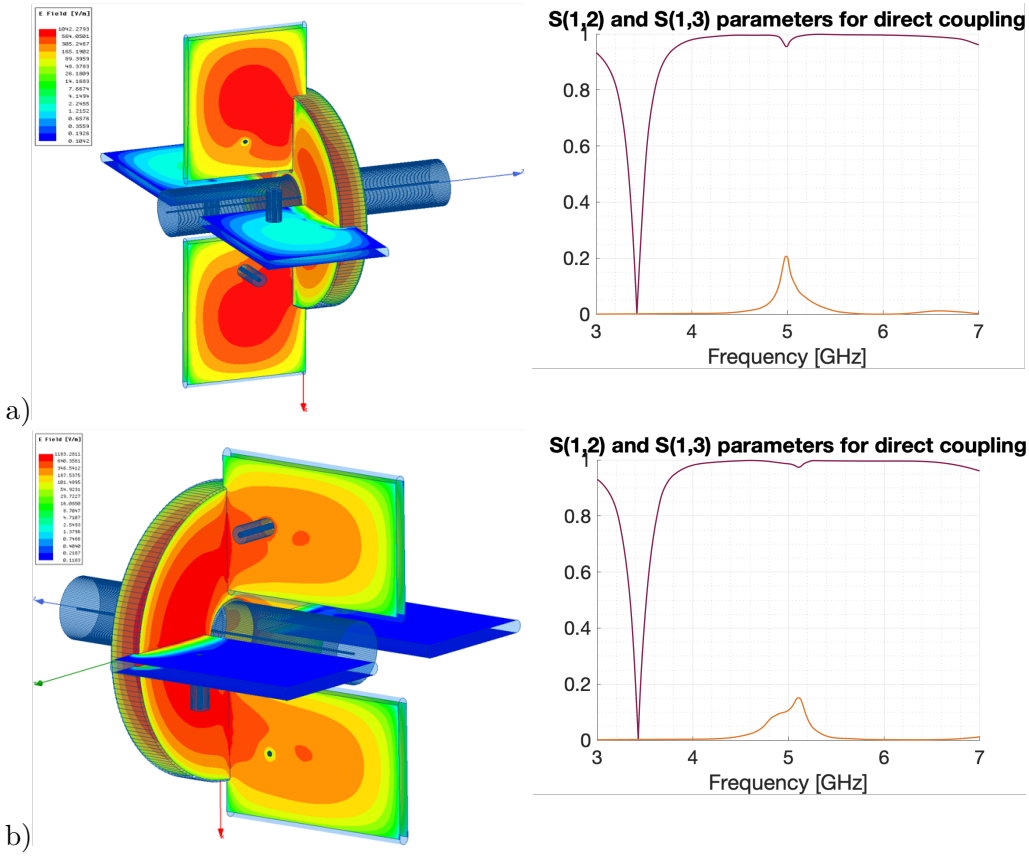

Figure 4.3. Different layout of the coupling waveguides to the 5.1 GHz prototype postion cavity and corresponding transmitted signal of dipole mode from the beampipe to the coaxial couplers for the 5.1 GHz postion cavity. The range of scale for a) is [0.1-1042] and for b) [0.1-1183]

put along with the beam tube is employed [34].. In this simulation, three waveports are used, two to denote the beam tube entrance and exit, and by the third one, a transverse cut of the coaxial feed-through is assigned. Consequently, the |S(1,2)| parameter for the monopole mode is transmitted from one end of the beam pipe to another without any loss; this means that the waveguides successfully reject it. However, for the dipole mode, one can observe the amount of the signal coupled out from the position cavity.

Hence, the advantage of a layout with 3mm waveguides is clearFigure 4.4, as in mechanical simplicity as in performance.

4.2 Optimizing design

After the prototype conceptual design was obtained, separate parts still need to be tuned to match the required properties and deliver optimal performance. Although the cavity beam position monitor can be considered as a system, where one component/dimension variation causes changes to other parameters, one can still divide the whole system into separate parts and start the design process to unite them in

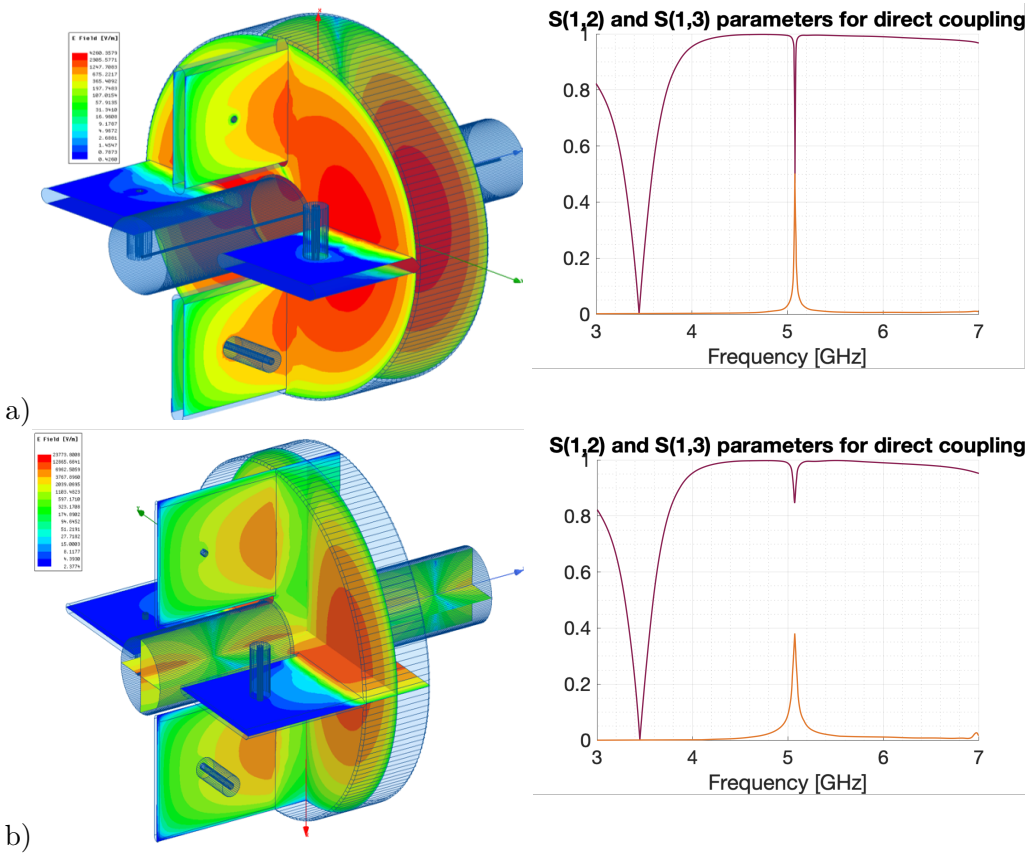

Figure 4.4. Different layout of the coupling waveguides to the 5.1 GHz prototype postion cavity and corresponding transmitted signal of dipole mode from the beampipe to the coaxial couplers for the postion cavity using abve cut-off rectangular waveguides. The range of scale for a) is [0.4-4200] and for b) [2.3-23772]

one particular layout then.

The position cavity radius was set to the working frequency using Equation 2.14 and optimized with the help of simulation software [35]. To determine the optimum position cavity length, which will provide sufficient output voltage for the required spatial resolution, corresponding simulation and long enough decay time τ, the output voltage dependence on the position cavity length with quality factor was set up. Figure 4.5.

As a result, it was clear that one needs to compromise between the quality factor and output voltage amplitude. As the length of the position cavity, 5 mm, was chosen. Although a shorter cavity provides a higher voltage at the coaxial output, the unloaded quality factor Q_0 becomes very low, and in order to have a loaded quality factor Q_L around 450-500, one will need to decrease the waveguide length, the dimension that has the most influence on the coupling between the position cavity and waveguide, which ,on the other hand,will affect the signal coupled out from the cavity.

The coupling four rectangular waveguides might behave as rectangular resonators if mismatching in the waveguide-coaxial transition occurs due to the residual power

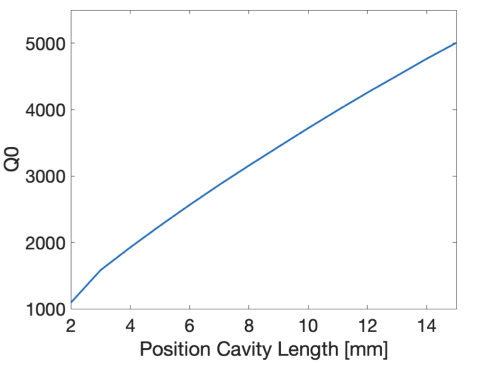

Q0 dependence on the position cavity length variation.

Output voltage Vout dependence on the position cavity length variation.

Figure 4.5. The position cavity parameters dependence on the resonator length variation.

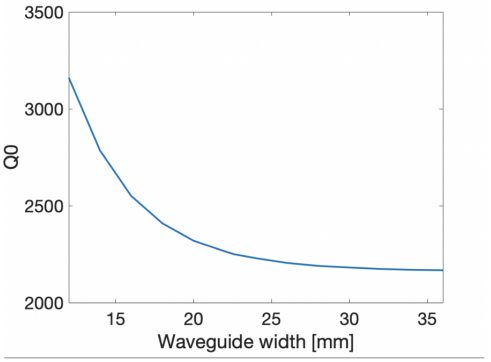

Q0 dependence on the waveguide width variation.

Vout dependence on the waveguide width variation.

Figure 4.6. The simulation results of the waveguide dimension optimization.

reflected by the waveguide-coaxial transition. Thus, the spurious modes have a resonant frequency that must be far away from that of the signal of interest. However, due to the waveguide dimensions, the resonances appear above the dipole mode.

The waveguide dimensions were determined through optimization, except the waveguide height, which was decided according to the Figure 4.4 results and is equal to 3 mm.

The waveguide dimensions are 21.57 mm×3 mm×22.6 mm. The aperture between the position cavity and the waveguide is 21.57 mm×3 mm. Hence, if the coupling needs to be adjusted, changing the 21.57 mm length will be most effective.

The position cavity dipole frequency is 5.1 GHz, located below the TE_{101} and TE_{102} resonant frequencies of the waveguide. Thus, the rectangular cavity's resonances do not affect the signal of interest because they will be filtered away by the electronic circuitry band-pass filter, centered at 5.1 GHz.

From Figure 4.6 one can notice that the waveguide's width is chosen at the point where the growth of the output voltage or the reducing unloaded quality factor gets saturated.

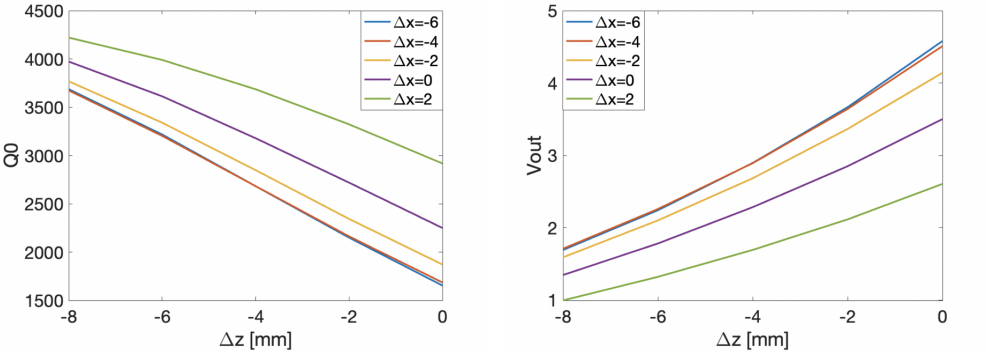

Quality factor dependence on the variation of z and x.

Vout dependence on the variation of z and x.

Figure 4.7. Coaxial port position variation influence on the output voltage and quality factor. The zero on the axis is the position where it is located in the original design Figure 4.8

.

Since the position cavity and waveguide dimensions are determined, one needs to pick a suitable position for the coaxial feed-through. Consequent simulations were set up.

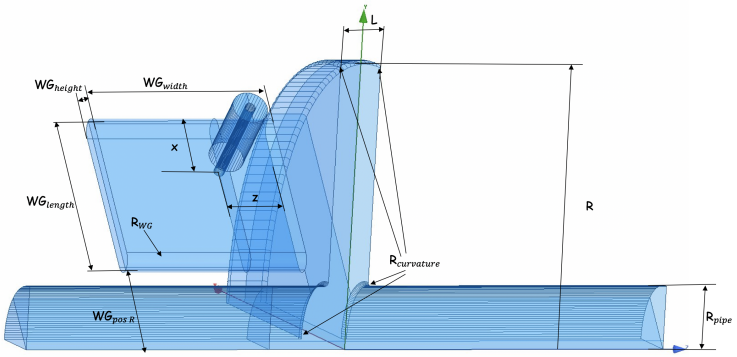

Figure 4.8. The position cavity's optimized design

As a starting position, in simulations Figure 4.7, for coaxial antenna across the x direction middle point of the waveguide was chosen. Different criteria were stated for the z direction since this parameter is responsible for the monopole mode tail amplitude. Although the tail signal's amplitude is on the order of 1-3 μV, one has to remember that this value will increase significantly due to the possible mechanical errors. However, placing the antenna further from the cavity opening will also reduce the dipole mode signal.

For the coaxial port position, we got 7 mm from the connection point of the position cavity and 6.3 mm from the upper wall of the waveguide. The unloaded quality factor of this particular layout of the position cavity is 2250, and the coupling constant β is equal to 4, which means that for the loaded quality factor Q_L we have 450. The output voltage for a 1 mm offset beam carrying a 1 nC charge on the perpendicular port to the offset is 4.9 volt. For a beam that crosses cavity with

Table 4.2. Dimension values for the 5.1GHz prototype position cavity.

Dimmension	Value[mm]
Position Cavity Radius R	34.07
Position Cavity Length L	5
Waveguide Length WG_{length}	21.57
Waveguide Width WG_{width}	22.6
Waveguide Height WG_{height}	3
Coaxial Position x	6.3
Coaxial Position z	7

Table 4.3. Dimension tolerances to the 1mm change for the 5.1GHz prototype position cavity.

Dimmension	Q_0 Variation [%/mm]	Frequency shift [MHz/mm]
Position Cavity Radius R	1	137.77
Position Cavity Length L	12	-28.06
Waveguide Length WG_{length}	-5	-4.2
Waveguide Width WG_{width}	-0.87	-0.12
Coaxial Position x	13	-0.48
Coaxial Position z	9	0.45

1° trajectory with respect to the central axis z and crossing it at the center of the cavity, carrying 1nC, at the corresponding port, we will get output voltage, which will be equal to V_{110}^{angle}=0.08. Consequently for $\frac{V_{110}^{angle}}{V_{110}^{out}} = 0.0163$. These properties seem reasonable for the requirements of EuPRAXIA@ SPARC_LAB project.

Since all of the dimensions and optimal values for the design Figure 4.8 are determined Table 4.2, one can evaluate the prototype's sensitivity to 1mm change for the dimensions that might have a significant influence on the resonance frequency and the quality factor Table 4.3. By doing so, one can approximate how sensitive is the overall design, and which dimensions need much more attention to precise sizing while manufacturing.

As expected, the most influence on the frequency has the resonator's radius; the change in radius by 1 mm causes the shift in resonance frequency for dipole mode by 137.77 MHz, second comes the cavity length. However, the quality factor is sensitive to resonator length and coaxial antenna separation from the waveguide wall; 1 mm shift results in a corresponding shift in quality factor, 12 % and 13% respectively.

After output voltage amplitude was obtained for a bunch with 1 nC charge and 1 mm offset from the cavity center, a time-dependent signal was simulated Figure 4.9, according to the equation

$$V(t) = V_{out} \cdot e^{-t/\tau} \cdot \sin(2 \cdot \pi f t) \tag{4.1}$$

where V_{out} is the output voltage amplitude, t is time variable, τ excited signal's decay time, f resonant frequency.

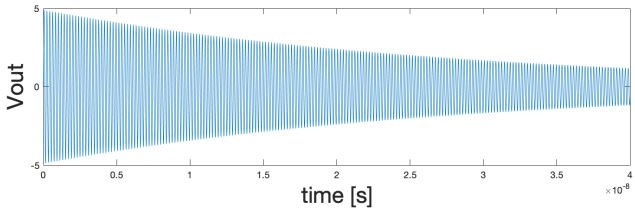

Figure 4.9. Simulation of the cBPM output signal on the coaxial ports is associated with the dipole mode's excitation. The signal is a sinewave, decaying in time, the amplitude is proportional to the beam charge and offset of the bunch. The parameters that define the signal (frequency f and decay constant τ) depend on the position cavity's geometry and its Q_L. The simulation is based on the parameters of the cBPM discussed in this section.

4.3 Wakefield simulation results

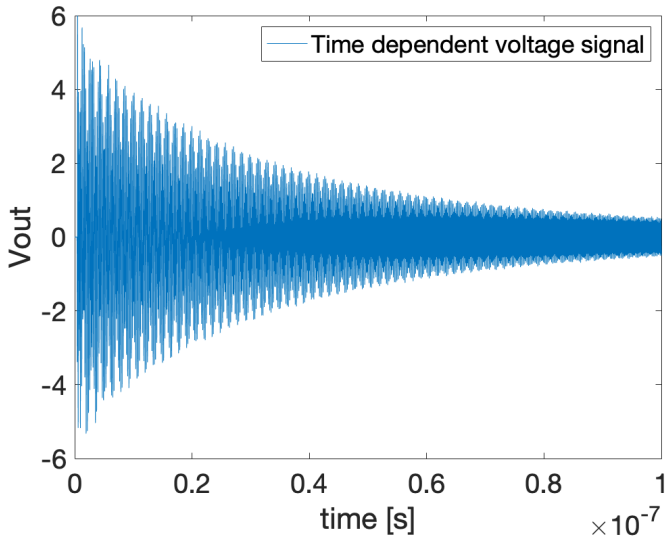

Figure 4.10. Output voltage signal coming out of one of the ports on x axis, with a 1 mm beam offset in y.

Using a wakefield solver gives a possibility to simulate the cavity's response to excitation with a charged particle bunch traveling through the beam pipe compared to the excitation on the ports used in the S-parameter simulation.

By doing lossless simulations, we could retrieve both the external and loaded Q values.

For the lossless simulation, CST was used to check for consistency of the results. Both codes, HFSS [35] and CST [36], gave very similar results, giving us confidence that they are accurate.

The beam simulated was a 1mm long gaussian pulse containing 1nC of charge. By moving the beam's position in the beam pipe, we could determine the effect of an asymmetric input on the structure.

Figure 4.11 shows the typical signal coming out of one of the ports, with a 1 mm

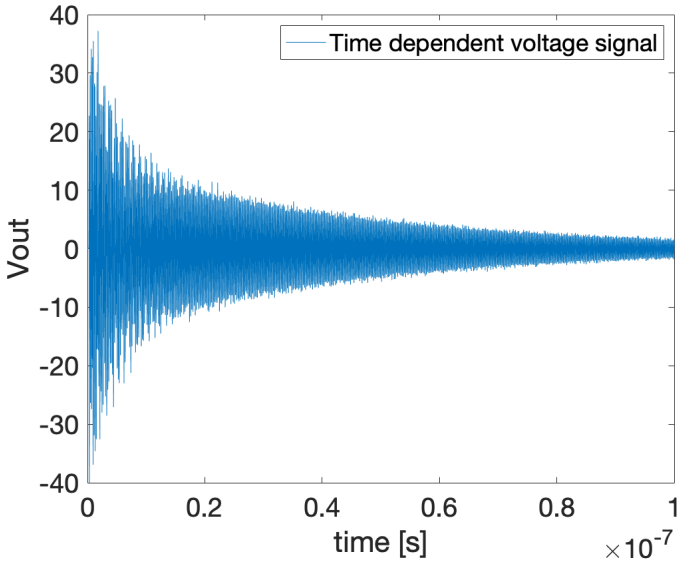

Figure 4.11. Output voltage signal coming out from the reference cavity, with a 1 mm beam offset in y.

beam offset in y. Figure 4.10 shows the voltage signal coming from the reference cavity.Usually, the signals are composed of different modes with different excitation amplitudes and with different decaying rates.

Indeed, taking the wake impedances Figure 4.12, we can see the prototype's resonance mode frequencies [25]. The dominant mode frequency was 5.1 GHz, corresponding to the lowest order dipole mode.

When the beam is only offset in either x or y, it was the only significant signal. However, when the beam was off-axis in both dimensions, then an additional peak at 7.02 GHz appeared. This response is a signature of the quadrupole mode: a beam offset in x or y only produces a symmetric field concerning the waveguides and so does not couple. However, when the beam is offset in both x and y, the symmetry gets broken, and the quadrupole mode is generated, some part of which is able to couple out into the waveguide.

4.4 Mechanical implementation

A prototype of the 5.1 GHz monitor is considered to be made of copper for laboratory measurements. It consists of three parts: resonator body, upper and lower cover. The resonator body contains the Position cavity with four coupling waveguides and the reference cavity, designed to have a shim. The resonator body was made of one part because the waveguides can then be manufactured by milling. Since the overall mechanical design is simplified, the clamping method was considered to be more beneficial than brazing to assemble the complete object. As we know, for example, RF accelerating structures are generally being manufactured by machining the different components through high precision lathes with milling machines. Then these copper components are brought together by brazing.

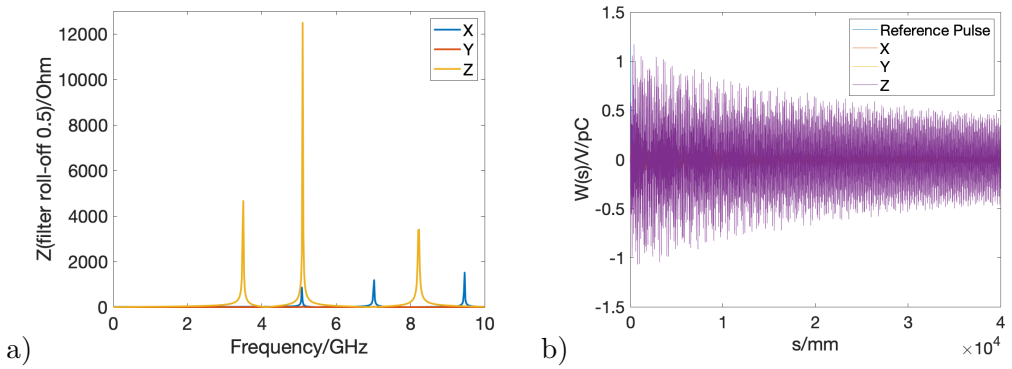

Figure 4.12. a) Wake impedance for the bunch, carrying 1nC charge with 1 mm offset b) Wake potential 40 m long

The brazing process is a metal joining process in which two metal parts are bonded together by melting an alloy that, at high temperature (typically above $800 - 900°C$), flows into the gaps between the parts to joint by capillary action. At each brazing step, a lower melting point alloy has to be used to avoid breaking previous brazing. In order to avoid oxidation throughout the described process, large and expensive vacuum furnaces are utilized. This process increases copper ductility, reducing copper annealing.

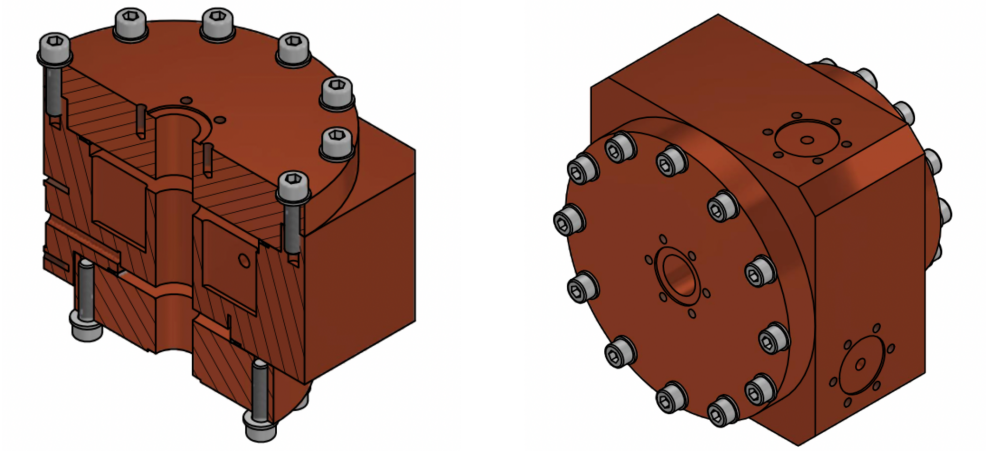

Longitudinal cut of the assembled prototype.

Assembled prototype.

Figure 4.13

During each brazing step, the parts undergo high mechanical and thermal stresses ($> 800°C$) due to the high temperature. Summarizing the brazing process, we can note several drawbacks as the risks of a failure of the brazing process are not negligible (vacuum leaks, damages, etc.). Besides, once the device is assembled and brazed, it is no longer possible to modify any geometrical dimension that does not appear on the outer faces of the device if one does not break the object. Hence, the brazing method does not allow device construction parts to be changed once the brazing

process is finished.

Due to all the reasons that are listed above, we can say that it might be costly. At the end of the process, the copper is "soft" since it has lost its mechanical hardness. Besides, in the case of RF accelerating structures, breakdown-rate studies (BDR) in C-band indicated that by avoiding the copper annealing associated with the high temperatures involved in the brazing process, the BDR probability could be reduced [46].

For all these reasons, a new fabrication method called the gasket-clamping technique has been developed at the INFN-LNF laboratories [33]. It avoids the brazing process in the structure fabrication by using special RF-vacuum gaskets to join the different machined parts. Hence, these parts are clamped together, employing screws radially, disposed around the cells. This technique has been successfully applied to realize both the new SPARC LAB 1.6 cells RF gun [38] and the ELI-NP-GBS. The prototype's overall design and realization goal are to demonstrate this technique's feasibility to manufacture an entire cBPM structure. The method makes it possible to change or replace including parts of the device, even after the tests that will be performed on the fully assembled device. This approach can also have a substantial scientific and industrial impact worldwide since, in principle, all companies with a resource to machine with high precision copper components will be able to fabricate a cBPM.

The upper or lower caps close the position and reference resonator and are screwed together with the resonator body. Directly coupled feed-throughs, different from the 6.1 GHz monitor, were used to couple the monitor signals. The direct coupling was implemented because of its simplicity, although it requires an exact calculation and a precise placement of probe due to its rather significant influence on the quality factor and output voltage.

In this chapter, the design of the cBPM is presented, putting in evidence the connection between mechanical constraints and electromagnetic parameters.

4.5 Study of fundamental mode coupling

The waveguide design that couple the cavity resonant fields out to the coaxial ports has a geometry that enhances the coupling between the waveguide TE_{10} mode and the cavity TM_{110} dipole mode and rejects the coupling with the cavity monopole modes. Thus, the waveguides are a first stage filter of the common-mode coupling. A second stage filtering is done in the BPM electronics with passband filters, as the frequency distance between the dipole mode and the closest monopole mode (TM_{010}) is larger than 1 GHz. Even if the common-mode coupling is ideally zero, there is always some residual coupling due to the pickup's mechanical tolerances .

One particular cause of residual common-mode coupling is deviations of the waveguide angles Figure 4.14 and shifts due to manufacturing errors/tolerances of the pick-ups. The plots displayed above show the output voltage at the cavity ports at the working frequency caused by the TM010 mode, for the case of possible manufacturing errors for the mechanical position and angle of the waveguides.

Figure 4.15 plot represts common mode out-put voltage, in case when the waveguides are not orthogonal to the position cavity. In conclusion, these plots

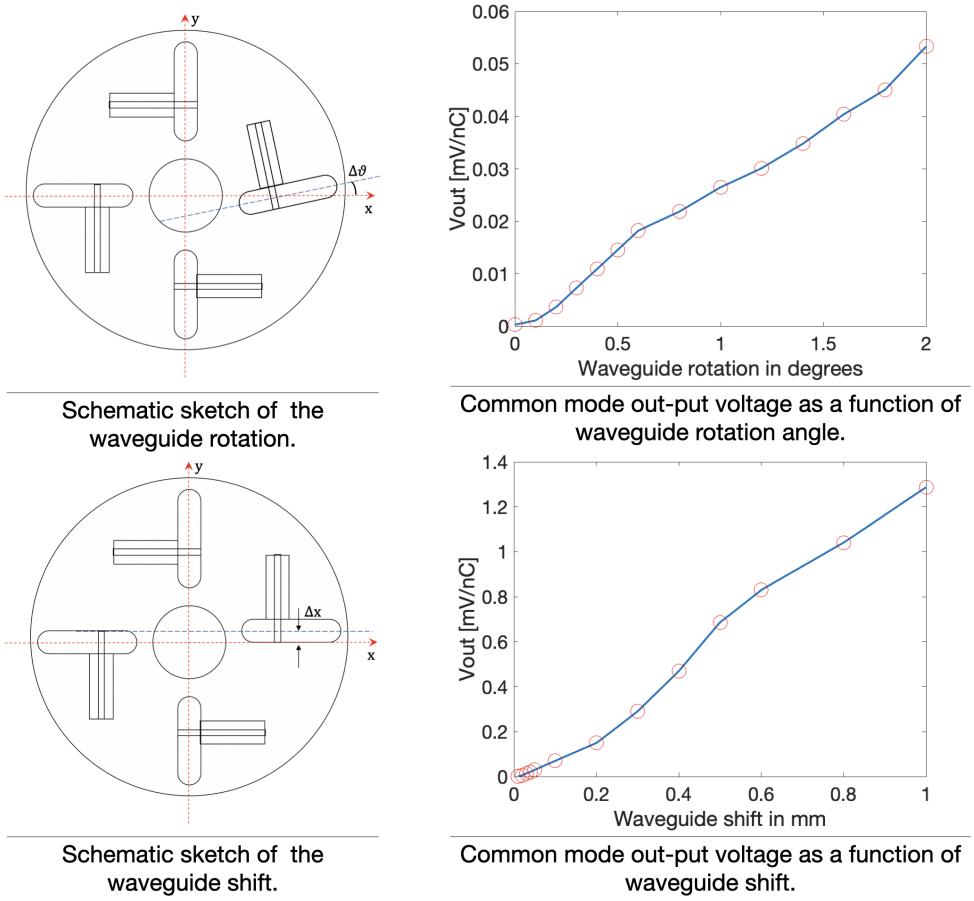

Figure 4.14. Simulated output signal, generated by 1nC, 1 mm offset beam, due to TM_{010} coupling as a function of waveguide misalignments.

determine the waveguide position's tolerances and angle errors for a given acceptable maximum common-mode signal. The ratio of sensitivity and error converges to a constant value when the position error converts to zero (or a realistically small value close to zero).

4.6 Study of diploe mode coupling to orthogonal port

Another undesired effect caused by manufacturing tolerances is the coupling between the horizontal and vertical planes. Ideally, a beam crossing the cavity with a pure horizontal (vertical) offset should produce a pure horizontal (vertical) output. However, the asymmetries introduced in the geometry by mechanical fabrication tolerances cause coupling between planes. The most potent sources of orthogonal coupling are also due to waveguide alignment errors. The main difference to the common-mode coupling is that even symmetrically perfect structure has some residual coupling between orthogonal ports, due to the quadrupole mode TM_{210}.

The waveguides strongly couple this mode, and as in contrast to the dipole mode, cannot distinguish horizontal and vertical beam offsets. Due to the very low beam

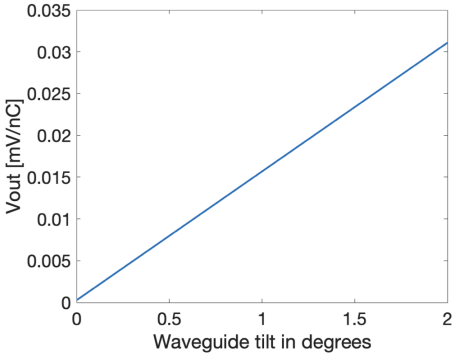

Figure 4.15. Simulated output signal, generated by 1nC, 1 mm offset beam, due to TM_{010} coupling as a function of waveguide tilt.

Table 4.4. Dimension tolerances to 1 mm change for the 5.1GHz prototype reference cavity

Dimmension	Value	Deviation, [MHz/1 mm]	Q variation [%/mm]
Reference Cavity Radius R	22.71	-221	5.6
Reference Cavity Length L	9	25.43	20
Trench Radius r	21.71	-315.38	-26
Reference Cacity Effective Length G	4	-175	-22
Distance between cavity wall and coaxial coupler D	2.6	3.5	-30

coupling impedance of this mode, the residual orthogonal coupling has a negligible impact on the position measurement. Figure 4.16 shows dipole mode coupled out on orthogonal port, obtained for a purely parallel beam offset, for different waveguide alignment errors.

4.7 5.1 GHz reference cavity

An induced dipole mode in the position cavity provides a signal that contains information about beam offset from the central axis, but one still needs a reference signal. The latter is needed for the normalization and getting the starting phase of the induced field in the position cavity. It gives the sign of displacement: when the beam is left, the system can be set up to give negative polarity. The signal becomes zero while the beam is centered and changes the phase by 180° when it moves to the right.

As in many resonant monitors, we also decided to use an additional circular cavity. As a reference signal, the reference cavity's TM_{010} mode is excited. This additional cavity measures the bunch charge and yields a phase difference. For convenience, the reference cavity's fundamental mode is often close to the position cavity's dipole-mode.

The following geometry displays Figure 4.17 the excited reference cavity. The cavity dimensions notations are displayed in Figure 4.17. It consists of a particular pillbox where the antenna is inserted in the bulge. In general, the insertion depth of

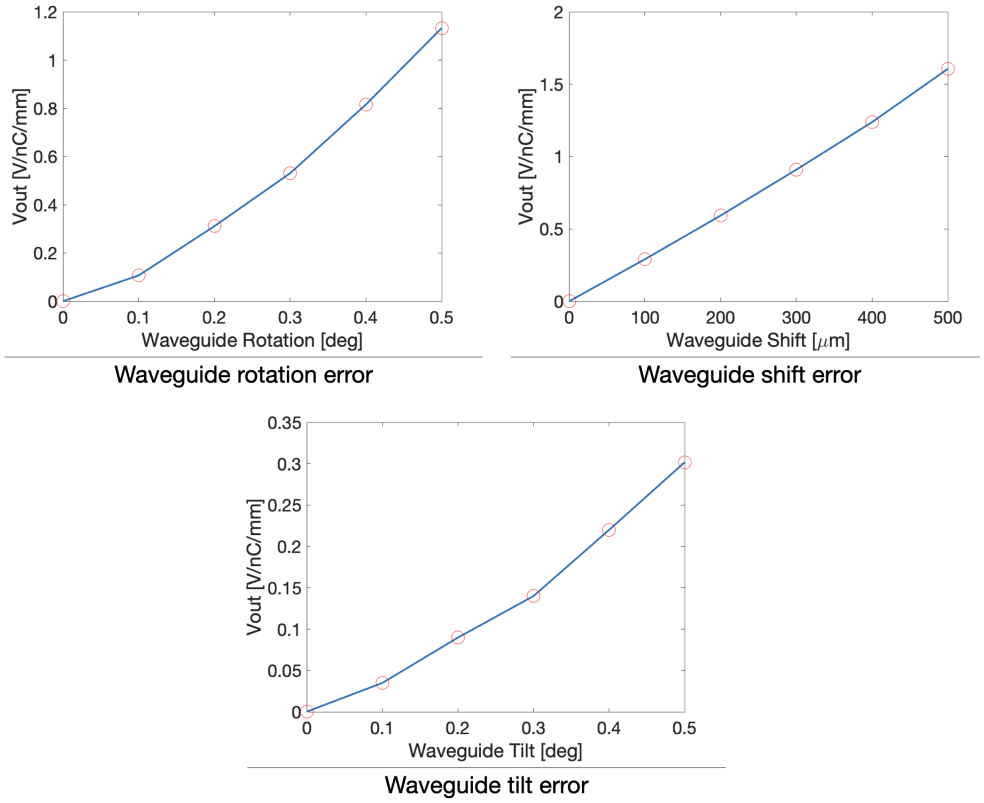

Figure 4.16. Dipole mode coupling to orthogonal port as a function of waveguide angle, position and tilt errors.

the antenna in the bulge determines the desired output signal level. In particular, the closer the antenna end is to the cavity wall, the higher the output signal amplitude becomes. This parameter also influences the loaded quality factor Q_L of the reference cavity. The antenna is mounted on the opposite wall in the bulge to reduce the variable parameters. The reference cavity's RF properties are determined by the height of the trench with the gap between the antenna and cavity wall.

The working frequency of the reference cavity is the same as the dipole-mode frequency of the position cavity, 5.1 GHz. The cavity's main parameters are listed in Table 4.4. To define the dimensional tolerances, to be specified in the mechanical drawings, the cavity center frequency and quality factor sensitivities to the main geometrical dimensions have been calculated. They are reported in Table 4.4.

The distance between position and reference cavity must be sufficiently large to avoid crosstalk between the coaxial ports. The reference cavity port has a different transmission to position cavity ports at 0° and 90° angle because the reference cavity has only one coupler; this causes a field distortion, thus breaking the 90° rotation symmetry of the pickup.

While a 45° tilt of the reference cavity coupler would equalize the crosstalk in both planes, it was decided to have the coupler at 0°, resulting in having a 2dB more crosstalk in one plane (compared to 45° angle), but much lower crosstalk in the other plane.

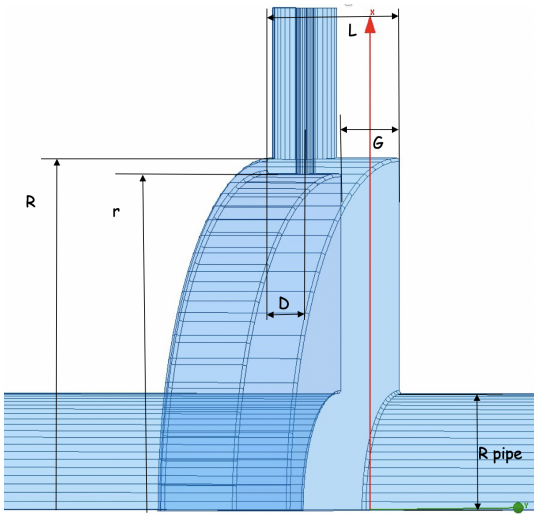

Figure 4.17. Schematic view of refernece cavity with geometrical indications

A distance of 32.5 mm between the two cavities is enough to reduce the crosstalk to a level that is negligible for the desired performance since the resulting cross-coupling isolation below -55 dB.

4.8 Resolution

In this section, a theoretical resolution of the prototype is evaluated by studying the BPM cavity's electrical performance using a simple analytical model and applying it to the C-band RF cBPM.

When a bunched beam of charged particles (electron/positron/etc.) passes through the cBPM cavity, it generates various electromagnetic modes, which can be formalized in a following way

$$V_{out}^{total}(5.1\text{GHz}) = V_{110}^{out} + V_{110}^{angle} + V_{010}^{out} + V_N \tag{4.2}$$

where, V_{110}^{out} is beam position signal, which is the in-phase component of TM_{110} mode [22].

V_{110}^{angle} is beam angle signal, which is 90 degree out-of-phase from the beam current. Even if the beam passes the cavity center: (r,z) = (0,0), it can still excite the TM110 mode due to the non-zero trajectory angle [21]. Since the beam couples to the electric field of negative polarity at z<0 and the positive polarity at z>0, the excitation voltage becomes 90° out-of-phase from the beam current. The output voltage for angle induced signal is determined similarly, as the position signal: voltage is integrated along the angled trajectory.

V_{010}^{out} is the leakage/tail of TM_{010} mode through the band-pass filter. Since the TM_{010} mode does not have a node point at the cavity center and the field pattern is almost flat, the electron beam always induces a constant voltage. Hence it is called "the common mode". In the case of the EuPRAXIA@ SPARC_LAB application, the electron beam has to be controlled to maintain the beam very close to the central axis, and the cBPM signal of TM_{110} mode becomes much smaller than the TM_{010}

Table 4.5. The main characteristics of the 5.1 GHz prototype

Parameter	Numerical calculation		
	TM_{010}	TM_{110}	Reference
f_{GHz}	3.419	5.100	5.100
Q_0	2800	2200	1400
Q_L	–	450	410
Damping time,τ ns		28.17	25.6
$\frac{R}{Q}$,Ohm	52	0.5	48
V_{out}	–	4.9 $V/nC/mm$	36 V/nC
angle/position signal ratio [deg/mm]	–	0.0163	–
Theoretical resolution	–	12.15 nm	–

mode. Therefore, even a very small leak of TM_{010} mode can deteriorate the BPM accuracy.

By the last term, V_N, thermal noise in the detector circuit is denoted. The thermal noise in the head amplifier limits the position resolution. The equivalent thermal noise is

$$V_N = \sqrt{4kT\Delta f R N_F} \tag{4.3}$$

Here, k is the Boltzman constant, T is the absolute temperature (K), Δf is the bandwidth of the signal (Hz), R is the circuit resistance (Ω), and N_F is the noise figure of the head amplifier.

For the bandwidth of the signal we have

$$\Delta f = \frac{f_{resonance}}{Q_{loaded}} = 11.3\,\mathrm{MHz} \tag{4.4}$$

As the absolute temperature, room temperaturre is considered $T = 293K$. For circuit resistance R we have 50 Ω. N_F depneds on the particular read-out electronics system, for simplicity we will just consider it as equal to 10. Hence, for last member of Equation 4.2 we get V_N=9.5781 $\times$ 10^{-06}

For the output signal induced by the tilted trajectory of the bunched beam V_{110}^{angle}, we consider this term equal to 0, assuming that bunch trajectory is paralell to the central axis.

As for the monopole mode leakage, one can assume the output signal for the minimal mechanical errors, resulting in an additional 50 μ V contribution in total V_{out}^{total}.

To evaluate the theoretical resolution, V_{110}^{out} should be larger than the sum of the other terms.

$$V_{110}^{out} = V_{110}^{angle} + V_{010}^{out} + V_N \tag{4.5}$$

The output signal is linearly dependent on the bunch offset; this means that one can represent V_{110}^{out} as a multiply of offset δx and a. Here a represents the coefficient, which is related to the bunch charge and can be determined from Equation 2.24

$$a \cdot \delta x = 5.9578 \times 10^{-05} \tag{4.6}$$

The relative displacement of the bunch will be sensed if V_{110}^{out}>5.9578×10^{-05}. Finally, for δx we get $\delta x = 12.15$ nm.

Usually, a system using one pick-up antenna is followed by a band-pass filter. Read-out electronic systems that are usually employed in the case of cavity beam position monitors will be discussed in the following chapter. In this equation, the noise signal limits the spatial resolution of the cBPM system, while the TM_{010} mode signal causes an electrical zero-point shift. It also causes saturation of the head amplifier and limits the dynamic range.

Chapter 5

Conclusion and Outlook

An assemblage of procedures to design a C-band RF cavity BPM for electron accelerators with low repetition rate bunches is displayed in this thesis. The required fundamental study topics, such as a mechanically less advanced prototype design, possible manufacturing flaws, affecting the monitor's RF properties, and decreasing its performance was studied. The analysis of these topics performed in detail with different simulation platforms.

5.1 A prototype with a working frequency of 6.1 GHz

As reviewed in Chapters 3 and 4, different designs, which meet project requirements, were studied.

A prototype with a working frequency of 6.1 GHz and length, dimension across the beampipe, $\approx$ 90mm. To meet the requirement regarding decay time $\tau \approx 30$ ns, the position cavity length was set to be 8 mm. Loaded quality factor Q_L is 1019. The width of the coupling slots between the waveguides and the position cavity is 1.5 mm. The cavity radius limits the slot length, resulting in limited coupling coefficient $\beta = 3$ for dipole mode.

The coaxial load position on the short-circuited waveguide was optimized to transmit the induced dipole mode signal more effectively. For the coupling method, capacitance coupling was chosen. Due to its much looser tolerance concerning the spacing between the flat bead and the waveguide wall. That is 0.7 mm instead of 0.22 in the case of using just a wire. The bead's geometrical shape was like a pill, with slight rounding on the edges, 0.5 mm as a curvature radius, 2 mm as a bead radius itself, and 1.2 as height. The $|S_{12}|$ and $|S_{11}|$ parameters at 6.1 GHz are respectively $\simeq 0.998$ and 0.003.

Simulations regarding fabrication errors and evaluating the mechanical tolerances of the device were performed. We observed that orthogonal port isolation was influenced more by the coupling slot rotation than by its shift from the symmetric axes. Slot rotation simulated gap from 0 to 2°. Isolation was below -30 dB, even when the slot was inclined by 0.5° to its symmetric axis. The isolation remained below -40 dB even if the slot shift from its ideal position was about 1 mm.

A beam crossing the resonator at an angle concerning the resonator axis produces a signal at the working frequency even if the average trajectory is centered. By

division of angle signal to the position offset voltage $\left|\frac{V_{angle}}{V_{position}}\right| = 0.052$

This monitor's sensitivity for a bunch with 1 nC charge and 1 mm offset from the central axis is 2.3 V/nC/mm.

5.2 One cavity cBPM design

When this design was prepared, the longitudinal size of cBPM was one of the crucial parameters. Due to this, we started studying cBPM design with only one cavity. Single cavity BPM needs a more complicated and expensive read-out electronic system and more tight mechanical constraints. Indeed such devices will exploit two different modes of the same cavity that must have a fixed frequency difference; tuning such difference can be extremely difficult and impractical. It was decided to mention it in a thesis as a possible solution, especially when longitudinal size is critical. Even though the RF design provides the same order of magnitude output voltage for dipole mode, treating the signal gets very complicated from the read-out electronics point of view. Currently, the number of cBPMs on the EuPRAXIA project reduced down to only 2. Thus, the device's longitudinal dimension is not worth a complicated read-out electronics system; hence, this design is currently no longer considered for the EuPRAXIA project.

5.3 A cavity BPM design with a dipole mode frequency at 5.1 GHz

The spatial dimensions of the waveguide adapter, as the length of the position cavity L=5mm, have been chosen to reduce overall device length. The mechanical design was optimized to decrease performance degradation due to fabrication errors.

We use the direct coupling method to simplify the prototype design in terms of manufacturing. Simulations dedicated to improving the dipole mode signal transition from the position cavity to a coaxial coupler shoved that, placing the conductor near the upper wall of the waveguide concerning the electromagnetic center of CBPM increases its loaded quality factor up to $Q_L = 450$ with acceptable output voltage value $V_{out} = 4.9$ V/nC/mm. Determined Q_L gives a sufficient decay time $\tau = \frac{2*Q_L}{\omega_0} = 28.31$ ns to take averages of the signal with read-out electronics.

Since the position cavity length reduced to 5mm, the bunch angle sensitivity decreased even more than in the 6.1 GHz cavity case. By division of angle signal to the position offset voltage $\left|\frac{V_{angle}}{V_{position}}\right| = 0.016$.

Simulations showed that higher mechanical accuracy of the order of $10\mu m$ is required with cavity radius since its changing reflects dramatically on the resonance frequency of the dipole-mode $1mm \leftarrow 137\,MHz$. On the other hand, the coaxial load position significantly influences loaded quality factor Q_L.

The RF properties and the EM response of the cBPM design were evaluated by simulations using the Eigenmode, frequency-domain, and time-domain solvers of different simulation software. The simulation results from the solvers we cross-examined.

The time-domain simulation predicted the output signal sensitivity, from an electron bunch with 1 nC charge and 1mm offset, to be ≈ 4.9 V_{out}. We also simulated wake potential with the same bunch parameters, where the bunch length was, $\sigma_z =$ 5 mm. With the wake impedance simulation, we estimated how good is isolation between the position cavity and the reference cavity. The distance separating the cavities is 41.5 mm.

The S-parameter measurements performing a simulation with a wire placed 1mm offset from the central axis across the simulated vacuum part of the device showed that the transmission $|S_{13}|$ was up to 0.44, while the maximum reflection was -8.2 dB at one of the ports. The Q values calculated using the coupling constant "β".

Different fabrication errors, which can degrade the orthogonal ports isolation and cause the field's rotation, including generating the coupling with the fundamental mode, were studied by simulation recreating the possible issues.

The isolation amid ports was more sensitive to the waveguide adapters' rotation than their shifts from the symmetry axes. However, it did not result in a dramatic change of the resonant frequencies. At the dipole-mode frequency, the orthogonal port isolation, when they are orthogonal, is better than 50 dB. Never the less, if one of the waveguides is rotated by 0.2° to the symmetry axis, the output voltage that will cross-couple to this port will be 0.6 V/nC/mm. The sensitivity is much less to the waveguide shift, 0.03 V/nC/mm for 0.3 mm shift.

The device is assembled from three parts, using the clamping method.

In particular, the method implements the new realization technique, called the "Gasket-Clamping technique". The technique has developed at the INFN laboratory in Frascati [38]. This method allows the fabrication process to circumvent the brazing process by using special RF-vacuum gaskets that simultaneously provide the radiofrequency contact and vacuum sealing while the different manufactured parts are clamped together.

An enhanced understanding of the operating principle of a cBPM was developed by comparing different simulations. The simulation studies provided a detailed estimation of the influence of different fabrication errors on the performance of a cBPM.

The presented design of cylindrical cBPM is economical and efficient.

5.4 Outlook

Once the first prototypes will be fabricated, test-bench measurments and beam tests will be performed.

Such a new test-bench for cBPMs at SPARC-LAB at INFN-LNF was designed and will be used in the prototype tests.

The test-bench consists of three Cavity BPMs installed on independent stages and moveable in the transverse plane in both directions through remote movers.

Immediately after the three cBPMs, a stripline BPM [60] is also installed to perform comparison measurements.

The test bench aims to perform measurements on the manufactured cBPMs. The main reason for these is to investigate further the prototype presented in this dissertation and their properties, dealing with the new challenges related to beam

diagnostics for the EuPRAXIA.

Mechanical drawings

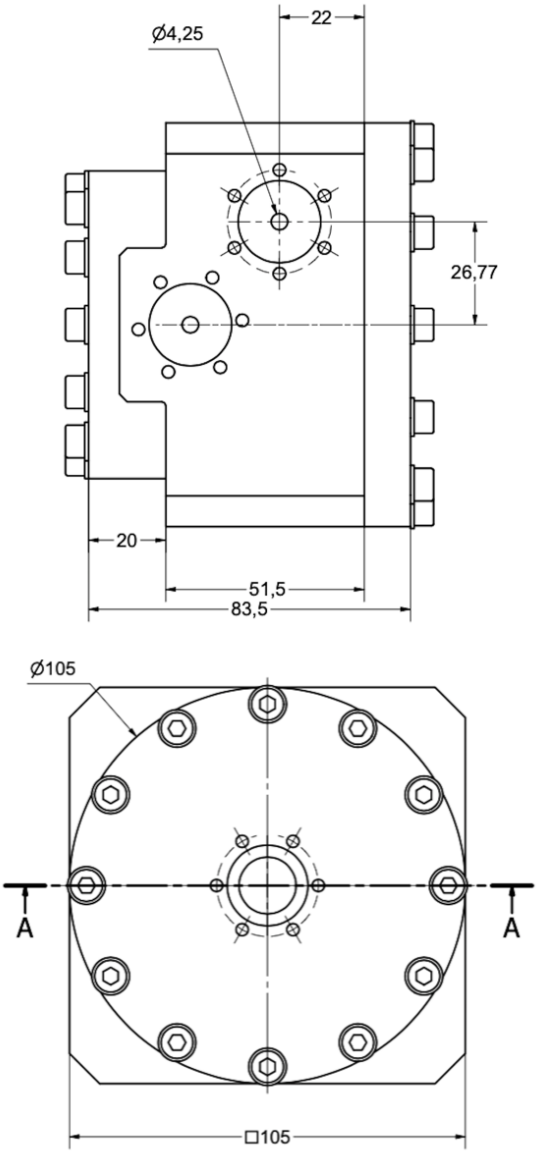

Figure .1. Mechanical drawing of the 5.1 GHz prototype, dimensions of the device. Dimensions are in mm.

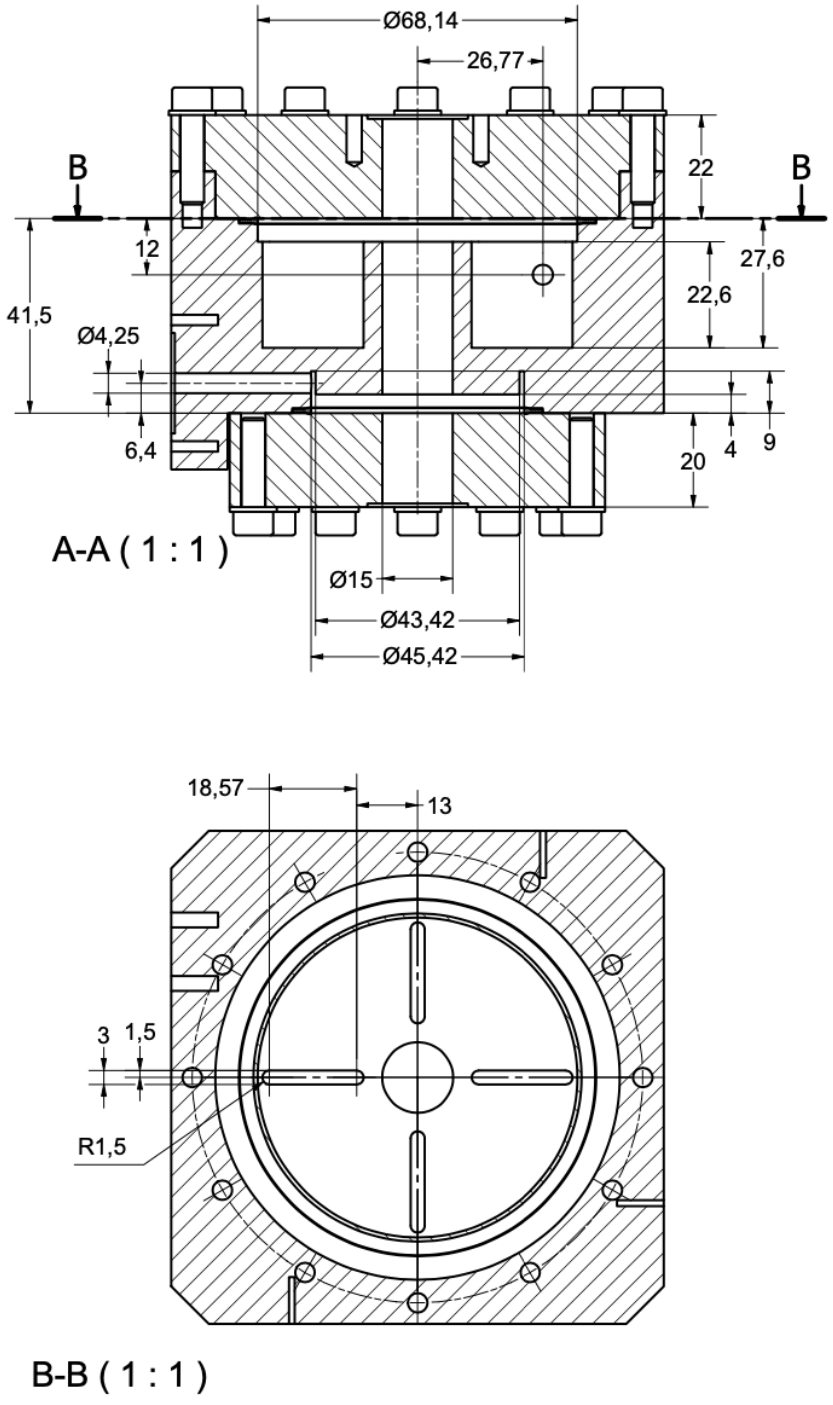

Figure .2. Mechanical drawing of the 5.1 GHz prototype. Dimensions are in mm.

Bibliography

[1] R. Lorenz Cavity Beam Position Monitors // Proc. of 8 Beam Instrumentation Workshop. Stanford, USA, 1998.

[2] V. Balakin, Bazhan A., Lunev P. et al. Beam Position Monitor with nanometer resolution for Linear Collider // Proc. of EPAC 1994. London, UK, 1994.

[3] M. Ross, Frisch J., Hendrickson L. et al. Very High Resolution RF Cavity BPM // Proc. of PAC 2003. Portland, USA, 2003.

[4] D. Boussard Beam Loading // Proc. of CERN Accelerator School. CERN 87-03. Geneva, Switzerland, 1987.

[5] A.S. Kalinin Diagnostika puchkov zaryazhennykh chastits s pomoshch'yu elektromagnitnykh datchikov v uskoritel'no-nakopitel'nykh ustanovkakh i elektronno-opticheskikh kanalakh: Avtoref. dis. ... kand. tekhn. nauk. Novosibirsk, 1985.

[6] V.V. Smaluk Diagnostika Puchkov Zarjazhennih Chastic v Uskoriteljah.

[7] D. M. Pozar. Microwave Engineering, pages 6-11,124,284–286. Wiley, New Jersey, 3 edition, 2005.

[8] E. L. Ginzton. Microwave Measurements, pages 343-349. McGraw-Hill, New York

[9] P. B. Wilson. Introduction to Wakefields and Wake Potentials. Technical Report SLAC-PUB-4547, SLAC, 1 1989.

[10] S. Walston, S. Boogert, C. Chung, P. Fitsos, J. Frisch, J. Gronberg, H. Hayano, Y. Honda, Y. Kolomensky, A. Lyapin, S. Malton, J. May, D. Mc- Cormick, R. Meller, D. Miller, T. Orimoto, M. Ross, M. Slater, S. Smith, T. Smith, N. Terunuma, M. Thomson, J. Urakawa, V. Vogel, D. Ward, and G. White. Performance of a High Resolution Cavity Beam Position Monitor System. Nuclear Instruments and Methods in Physics Research A, 578:1–22, 2007.

[11] W. Bruns. A Finite Difference Program with Reduced Memory and CPU Usage. In PAC 1997, number 9P118, 1997.

[12] K. Ko, A. Candel, L. Ge, A. Kabel, R. Lee, Z. Li, C. Ng, V. Rawat, G. Schussman, and L. Xiao. Advances in Parallel Electromagnetic Codes for Accelerator Science and Development. In LINAC 2010, number FR101, 2010.

[13] R. Garg. Analytical and Computational Methods in Electromagnetics, pages 233–280,355–444. Artech House, Boston, 2008.

[14] D. H. Whittum and Y. Kolomensky. Analysis of an Asymmetric Resonant Cavity as a Beam Monitor. Review of Scientific Instruments, 70(5):2300– 2313, 1999.

[15] W. H. Hayt and J. E. Kemmerly. Engineering Circuit Analysis, pages 431– 450. McGraw-Hill, New York, 2 edition.

[16] A. Lunin. High Resolution RF Cavity BPM Design for Linear Collider. In 8th DITANET Topical Workshop on Beam Position Monitors, CERN, Switzerland, 1 2012.

[17] N. Chritin, H. Schmickler, L. Søby, A. Lunin, N. Solyak, M. Wendt, and V. Yakovlev. A High-Resolution Cavity BPM for the CLIC Test Facility. In BIW 2010, number TUPSM32, 2010.

[18] F. Cullinan, Development of a Prototype Cavity Beam Position Monitor for the Compact Linear Collider, PhD Thesis, Royal Holloway, University of London 2014

[19] O.S.Milovanov, N.P.Sobenin, Technika Sverhvysokih Chastot, Atomizdat, Moscow, 1980

[20] N.Y. Joshi, Design and Analysis Techniques for Cavity Beam Position Monitor Systems for Electron Accelerators, Dissertation, Royal Holloway, University of London 2013

[21] T.Shintake, Proposal of Nanometer Resolution Beam Position Monitor, Draft

[22] T.Slaton at all, Development of Nanometer Resolution C-Band Radio Frequency Beam Position Monitors in The Final Focus Test Beam

[23] T.Shintake, Nanometer Resolution BPM Using Damped Slot Resonator, PAC95, Dallas, 1995

[24] W.Schnell, Common-mode rejection in resonant microwave position monitors for linear colliders, CERN-LEP-RF/88-41 CLIC Note 70, 1988

[25] I.Wilson at all, An Asset Test of The CLIC Accelerating Structure, CERN/PS 200-044 (RF) CLIC Note 443, 2000

[26] A. Lyapin, Strahllagemonitor fuer das TESLA-Energiespektrometer, Dissertation, TU-Berlin, Berlin, 2003.

[27] M. Ferrario, D. Alesini, M. P. Anania, M. Artioli, A. Bacci, S. Bartocci, R. Bedogni, M. Bellaveglia, A. Biagioni, F. Bisesto, F. Brandi, E. Brentegani, F. Broggi, B. Buonomo, P. L. Campana, G. Campogiani, C. Cannaos, S. Cantarella, F. Cardelli, M. Carpanese, M. Castellano, G. Castorina, N. C. Lasheras, E. Chiadroni, A. Cianchi, R. Cimino, F. Ciocci, D. Cirrincione, G. A. Cirrone, R. Clementi, M. Coreno, R. Corsini, M. Croia, A. Curcio,G. Costa, C. Curatolo, G. Cuttone, S. Dabagov, G. Dattoli, G. D'Auria, I. Debrot, M. Diomede, A. Drago, D. Di Giovenale, S. D. Mitri, G. Di Pirro, A. Esposito, M. Faiferri, L. Ficcadenti,

F. Filippi, O. Frasciello, A. Gallo, A. Ghigo, L. Giannessi, A. Giribono, L. Gizzi, A. Grudiev, S. Guiducci, P. Koester, S. Incremona, F. Iungo, L. Labate, A. Latina, S. Licciardi, V. Lollo, S. Lupi, R. Manca, A. Marcelli, M. Marini, A. Marocchino, M. Marongiu, V. Martinelli, C. Masciovecchio, C. Mastino, A. Michelotti, C. Milardi, V. Minicozzi, F. Mira, S. Morante, A. Mostacci, F. Nguyen, S. Pagnutti, L. Pellegrino, A. Petralia, V. Petrillo, L. Piersanti, S. Pioli, D. Polese, R. Pompili, F. Pusceddu, A. Ricci, R. Ricci, R. Rochow, S. Romeo, J. B. Rosenzweig, M. R. Conti, A. R. Rossi, U. Rotundo, L. Sabbatini, E. Sabia, O. S. Plannell, D. Schulte, J. Scifo, V. Scuderi, L. Serafini, B. Spataro, A. Stecchi, A. Stella, V. Shpakov, F. Stellato, E. Turco, C. Vaccarezza, A. Vacchi, A. Vannozzi, A. Variola, S. Vescovi, F. Villa, W. Wuensch, A. Zigler, and M. Zobov, "EuPRAXIA@SPARC_LAB Design study towards a compact FEL facility at LNF," Nuclear Instruments and Methods in Physics Research, Section A: Accelerators, Spectrometers, Detectors and Associated Equipment, 2018, issn: 01689002. doi: 10.1016/j.nima.2018.01.094.

[28] "EuPRAXIA@SPARC_LAB Conceptual Design Report," Tech. Rep. INFN - 18-03/LNF, 2018.

[29] M. Ferrario et al., "SPARC_LAB present and future," Nucl. Instrum. Meth. B, vol. 309, pp. 183–188, 2013.

[30] P. Walker et al., "HORIZON 2020 EuPRAXIA Design Study," in Proc. of International Particle Accelerator Conference (IPAC'17), Copenhagen, Denmark, 14-19 May, 2017, (Copenhagen, Denmark), ser. International Particle Accelerator Conference, Geneva, Switzerland: JACoW, May 2017, pp. 1265–1268, isbn: 978-3-95450-182-3. doi: https://doi.org/10.18429/ JACoW-IPAC2017-TUOBB3.

[31] EuPRAXIA website, http://www.eupraxia-project.eu/.

[32] D. Alesini et al., "Process for manufacturing a vacuum and radio- frequency metal gasket and structure incorporating it," Int'l patent appli- cation PCT/IB2016/051464 assigned to INFN.

[33] D. Alesini et al., "New technology based on clamping for high gradient radio frequency photogun," Physical Review Special Topics - Accelerators and Beams, vol. 18, 2015.

[34] F. Marcellini, M. Serio, M. Zobov DAΦNE BROAD-BAND BUTTON ELECTRODES

[35] "Ansys HFSS." Available online: http://www.ansys.com

[36] CST Studio Suite website, https : / / www . 3ds . com / products - services / simulia/products/cst-studio-suite/.

[37] Y. I. Kim, R. Ainsworth, A. Aryshev, S. T. Boogert, G. Boorman, J. Frisch, A. Heo, Y. Honda, W. H. Hwang, J. Y. Huang, E-S. Kim, S. H. Kim, A. Lyapin, T. Naito, J. May, D. McCormick, R. E. Mellor, S. Molloy, J. Nelson, S. J. Park, Y. J. Park, M. Ross, S. Shin, C. Swinson, T. Smith, N. Terunuma, T. Tauchi,

J. Urakawa, and G. R. White Cavity beam position monitor system for the Accelerator Test Facility 2

[38] D. Alesini et al., "Process for manufacturing a vacuum and radio- frequency metal gasket and structure incorporating it," Int'l patent appli- cation PCT/IB2016/051464 assigned to INFN.

[39] B. Walasek-Hohne, C. Andre, P. Forck, E. Gutlich, G. Kube, P. Lecoq, A. Reiter, Scintillating screen applications in accelerator beam diagnostics, IEEE Trans. Nucl. Sci. 59 (5) (2012) 2307–2312.

[40] A. Curcio, M. Anania, F. Bisesto, E. Chiadroni, A. Cianchi, M. Ferrario, F. Filippi, D. Giulietti, A. Marocchino, M. Petrarca, et al., Trace-space reconstruction of low- emittance electron beams through betatron radiation in laser-plasma accelerators, Phys. Rev. Accel. Beams 20 (1) (2017) 012801.

[41] F.Lohl,S.Schreiber,M.Castellano,G.DiPirro,L.Catani,A.Cianchi,K.Honkavaara, Measurements of the transverse emittance at the FLASH injector at DESY, Phys. Rev. Spec. Top.-Accel. Beams 9 (9) (2006) 092802.

[42] M. Migliorati, A. Bacci, C. Benedetti, E. Chiadroni, M. Ferrario, A. Mostacci, L. Palumbo, A. Rossi, L. Serafini, P. Antici, Intrinsic normalized emittance growth in laser-driven electron accelerators, Phys. Rev. Spec. Top.-Accel. Beams 16 (1) (2013) 011302.

[43] A. Rousse, K.T. Phuoc, R. Shah, A. Pukhov, E. Lefebvre, V. Malka, S. Kiselev, F. Burgy, J.-P. Rousseau, D. Umstadter, et al., Production of a keV X-ray beam from synchrotron radiation in relativistic laser-plasma interaction, Phys. Rev. Lett. 93 (13) (2004) 135005.

[44] G. Plateau, C. Geddes, D. Thorn, M. Chen, C. Benedetti, E. Esarey, A. Gonsalves, N. Matlis, K. Nakamura, C. Schroeder, et al., Low-emittance electron bunches from a laser-plasma accelerator measured using single-shot x-ray spectroscopy, Phys. Rev. Lett. 109 (6) (2012) 064802.

[45] S. Kneip, C. McGuffey, J. Martins, M. Bloom, V. Chvykov, F. Dollar, R. Fonseca, S. Jolly, G. Kalintchenko, K. Krushelnick, et al., Characterization of transverse beam emittance of electrons from a laser-plasma wakefield accelerator in the bubble regime using betatron x-ray radiation, Phys. Rev. Spec. Top.-Accel. Beams 15 (2) (2012) 021302.

[46] V.A. Dolgashev, J. Wang, RF design of X-band RF deflector for femtosecond diagnostics of LCLS electron beam, in: AIP Conference Proceedings, vol. 1507, AIP, 2012, pp. 682–687.

[47] E. Chiadroni, M. Bellaveglia, P. Calvani, M. Castellano, L. Catani, A. Cianchi, G. Di Pirro, M. Ferrario, G. Gatti, O. Limaj, et al., Characterization of the THz radiation source at the Frascati linear accelerator, Rev. Sci. Instrum. 84 (2) (2013) 022703.

[48] T. Maxwell, C. Behrens, Y. Ding, A. Fisher, J. Frisch, Z. Huang, H. Loos, Coherent- radiation spectroscopy of few-femtosecond electron bunches using a middle-infrared prism spectrometer, Phys. Rev. Lett. 111 (18) (2013) 184801.

[49] M. Heigoldt, A. Popp, K. Khrennikov, J. Wenz, S.-W. Chou, S. Karsch, S. Bajlekov, S. Hooker, B. Schmidt, Temporal evolution of longitudinal bunch profile in a laser wakefield accelerator, Phys. Rev. Spec. Top.-Accel. Beams 18 (12) (2015) 121302.

[50] R. Pompili, A. Cianchi, D. Alesini, M. Anania, A. Bacci, M. Bellaveglia, M. Castellano, E. Chiadroni, D. Di Giovenale, G. Di Pirro, et al., First single-shot and non- intercepting longitudinal bunch diagnostics for comb-like beam by means of electro- optic sampling, Nucl. Instrum. Methods Phys. Res. A 740 (2014) 216–221.

[51] C. Clayton, L. Serafini, Generation and transport of ultrashort phase-locked electron bunches to a plasma beatwave accelerator, IEEE Trans. Plasma Sci. 24 (2) (1996) 400–408.

[52] P. Forck, P. Kowina, and D.LiakinBeam position monitors. Gesellschaft fur Schwerionen for schung GSI, Darmstadt, Germany

[53] D. Lipka *et al.*, "Orthogonal Coupling in Cavity BPM with Slots", in *Proc. 9th European Workshop on Beam Diagnostics and Instrumentation for Particle Accelerators (DIPAC'09)*, Basel, Switzerland, May 2009, paper MOPD02, pp. 44–46.

[54] A. Molaee, M.Samadfam, M.Mohammadzadeh, Sharif University of Technology (SUT), Tehran, Iran Mehdi Shafiee, Iranian Light Source Facility (ILSF), IPM, Tehran, Iran GENERAL CONSIDERATION FOR BUTTON-BPM 5th International Particle Accelerator Conference IPAC2014, Dresden, Germany JACoW Publishing ISBN: 978-3-95450-132-8 doi:10.18429/JACoW-IPAC2014-THPME126

[55] A. Stella ANALYSIS OF THE DAΦNE BEAM POSITION MONITOR WITH A BOUNDARY ELEMENT METHOD DAΦNE TECHNICAL NOTE INFN - LNF, Accelerator Division Frascati, December 19, 1997 Note: CD-10

[56] F. Marcellini, M. Serio, A. Stella, M. Zobov DAΦNE broad-band button electrodes INFN Lahoratori Narionali di Frascati. Via E. Fermi, P.O. Box 13. I-00044 Frasrati (Roma), Iialy Nuclear Instruments and Methods in Physics Research A 402 (1998) 27-35

[57] G. Kube, Particle beam diagnostics and control, Proc. Int. Sch. Phys. Fermi **179**, 93-114 (2012) doi:10.3254/978-1-61499-129-8-93

[58] A.Cianchia, D.Alesini, M.P.Anania, F.Biagioni, F.Bisesto, E.Chiadroni, A.Curcio, M.Ferrario, F.Filippi, A.Ghigo, A.Giribono, V.Lollo, A.Mostacci R.Pompili L.Sabbatini V.Shpakov A.Stella C.Vaccarezza A.Vannozzi F.Villa Nuclear Instruments and Methods in Physics Research Section A: Accelerators,

Spectrometers, Detectors and Associated Equipment Volume 909, 12 November 2018, Pages 350-354 Conceptual design of electron beam diagnostics for high brightness plasma accelerator

[59] P. Forck et al., Proc. CERN Accelerator School, CERN-2009-05, p.187.

[60] A.Stella et al. "Stripline bpm with integral in-vacuo termination" Proceedings of 3rd Int. Particle Accelerator Conf. (IPAC'12), New Orleans, LA, USA, pp. 828-830, 2012.

List of Figures

List of Tables